Escola de Camins
Escola Tècnica Superior d'Enginyeria de Camins, Canals i Ports
UPC BARCELONATECH

TREBALL FINAL DE MÀSTER

Micromechanical Modelling of Experimental Shear Tests on Cylindrical Specimens of Masonry

Treball realitzat per:

Guillermo Lahuerta Piñeiro

Dirigit per:

Luca Pelà

Màster en:

Enginyeria de Camins Canals i Ports

Barcelona, 15 de juny de 2018

Departament d'Enginyeria Civil i Ambiental

Acknowledgements

First, I would like to express my gratitude to my research supervisor, Professor Luca Pelà, for his patient guidance, supervision and advice throughout the development of this master thesis. It was my privilege to work and learn from him.

Second, to all the professors that provided the necessary knowledge to overcome the difficulties found trough the master's degree. Also, to my classmates that made this experience much more enriching from a personal point of view. I wish them all the best in life.

Third, to my personal friends, Edgard, Javier, Mayte, Ana and Miranda, who supported me during all these hard years.

Finally, to my sister and to my parents, for providing me the best education they could afford. This is for you.

Abstract

Masonry is one of the most common materials widely used around the world in the construction of buildings, from ancient times to present. For this reason, the study of the mechanical behavior of masonry is necessary to preserve the integrity of existing and new structures.

Unfortunately, masonry is a very complex material since it is formed by different elements (brick and mortar). Due to this heterogeneity, its mechanical behavior is very difficult to predict. Among all the possible stress states, the one that involves most complexity is the shear stress, since it affects the weakest part of the masonry: the mortar-brick interface.

The objective of this thesis is to acquire knowledge of the behavior of masonry under shear loads, and more specifically, understand the behavior in the mortar-brick interface.

To do so, a numerical model capable to replicate the behavior of cylindrical masonry specimens in shear tests has been developed. This numerical model provides results in reasonable agreement with the ones obtained in two experimental campaigns carried out by different authors.

The results obtained with the model are presented and analyzed in detail. This allows to extract conclusions about the mechanical behavior of the brick-mortar interface in order to improve the existing knowledge in the literature about this phenomenon.

Finally, suggestions for future work in this field of research are presented.

Resumen

La obra de fábrica (o mampostería) es uno de los materiales más comúnmente utilizados en todo el mundo en la construcción de edificios, desde monumentos históricos en la antigüedad hasta edificios en el presente. Por esta razón, el estudio del comportamiento mecánico de la obra de fábrica es necesario para preservar la integridad de las estructuras, tanto existentes como futuras.

Desafortunadamente, la mampostería es un material muy complejo ya que está formado por diferentes elementos (ladrillo y mortero). Debido a esta heterogeneidad, su comportamiento mecánico es muy difícil de predecir. Entre todos los estados de tensión posibles, el que involucra una mayor complejidad es la tensión por cortante, ya que afecta a la parte más débil de la obra de fábrica: la interfaz mortero-ladrillo.

El objetivo de esta tesis es entender el comportamiento de la obra de fábrica bajo cargas de cortante, y más específicamente, comprender el comportamiento en la interfaz mortero-ladrillo.

Para ello, se ha desarrollado un modelo numérico capaz de replicar el comportamiento de muestras cilíndricas de obra de fábrica en ensayos de cizallamiento. Este modelo numérico proporciona resultados razonablemente en concordancia con los obtenidos en dos campañas experimentales llevadas a cabo por distintos autores.

Los resultados obtenidos con el modelo se presentan y se analizan en detalle. Esto permite extraer conclusiones sobre el comportamiento mecánico de la interfaz ladrillo-mortero de cara a mejorar el conocimiento existente en la literatura sobre este mecanismo.

Finalmente, se presentan sugerencias para trabajos futuros en este campo de investigación.

Content

Chapter 1. Introduction

1.1 Motivation of the thesis

Masonry is **one of the most ancient constructive materials** used for building structures all over the world. Although its applications and construction technologies have evolved over years, its construction technique is essentially the same: stack units (bricks) and bound them, typically with mortar.

The main keys for the success of masonry are the **ease of construction** and its **low cost**. Other factors that have contributed to its wide use are: aesthetics, durability, low maintenance, versatility and sound and thermal insulation (Lourenço, 1996).

Due to these good properties, masonry is one of the most common construction materials used for **buildings**. Furthermore, a large number of **historical monuments** were built with masonry hundreds of years ago, especially in countries like Spain or Italy. At that time, the construction criteria were only based on empirical rules and neither a normative nor structural knowledge were applied.

Therefore, the study of the mechanical behavior of masonry is necessary to preserve the **integrity of existing and future masonry structures**, both for practical and cultural reasons.

However, one of the main drawbacks of masonry is the **complexity** of the material due to its heterogeneity, non-linearity and discontinuities (see Figure 1). Besides, the way in which masonry is built (i. e., the number of joints and their position) has also a great impact in its performance. Because of this, it is very **difficult to predict and understand its mechanical behavior under different types of loads**.

Among all the possible stress states (compression, tension and shear), the one that involves most difficulty is **shear**, since it directly affects the weakest part of the masonry: the **mortar-brick interface** (see Figure 1). Unfortunately, the knowledge of the behavior of masonry under shear stresses is clearly lower in the literature than for compression. The response under shear loads is of special interest in cases of lateral loading conditions, like **winds or earthquakes**.

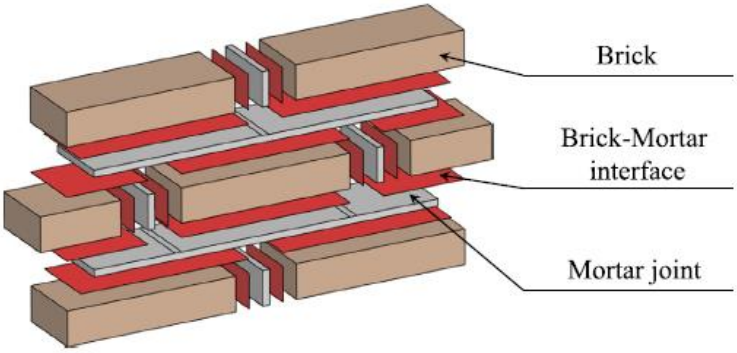

Figure 1. ***Masonry elements. Source: (Petracca, et al., 2017).***

To sum up, in order to guarantee the integrity of existing and future structures it is necessary to **improve the knowledge of masonry's behavior** under different types of stresses, and more specifically, address the **behavior of the mortar-brick interface under shear loads**.

1.2 Objectives

The objective of this thesis is to **acquire knowledge of the behavior of masonry under shear loads**. To do so, a numerical model capable to replicate the behavior of cylindrical masonry specimens in shear tests will be developed.

This numerical model is expected to obtain results in reasonable agreement with the ones obtained in experimental campaigns carried out by different authors (Pelà, et al., 2017 and Marastoni, et al., 2016). In these campaigns, the authors selected materials with low mechanical properties to simulate the masonry of **historical monuments**.

Obtaining a good correlation between the experimental campaign and the model will allow the author of this thesis to obtain conclusions about the way that **masonry responds to shear stresses**.

This will be helpful to obtain **valuable information about the behavior of masonry** that will increase the knowledge about this material, and hopefully, will help other researchers in the development of new models.

1.3 Methodology

The steps followed during the thesis are:

1. Collect information about the **state of the art** about the following topics:
    a. **Mechanical behavior** of masonry.
    b. **Failure criteria** of masonry.
    c. **Experimental tests** available to characterize the material.
    d. **Numerical models** available for the analysis of masonry.
2. Obtain the data from the **experimental campaigns** mentioned before.
3. **Develop and calibrate a model** to simulate the shear behavior in the brick-mortar interface of masonry cylindrical specimens.
4. Obtain the **results** of the model and analyze them to extract **conclusions about the behavior of masonry**.
5. Propose **suggestions for future work** in this field of research.

1.4 Outline of the document

The thesis is divided into 6 chapters:

- **Chapter 1**: In this chapter, the thesis is presented as well as the motivation, objectives and methodology to be applied.
- **Chapter 2**: This chapter presents the theory behind the principal topics that will be analyzed in detail along the thesis. More specifically, it is introduced the different mechanical behavior of masonry depending on the nature of the stress applied, the Mohr-Coulomb failure criterion, experimental tests available to characterize the mechanical properties of masonry and numerical models used in literature for the analysis of masonry.

- **Chapter 3**: In this section, the experimental campaigns carried out by Marastoni, et al., 2016 and Pelà, et al., 2017, are presented. These campaigns provide the experimental data necessary to calibrate the model.

- **Chapter 4**: In this chapter, the material model is presented, as well as the calibration procedure. Finally, the final model is presented.

- **Chapter 5**: The results obtained for the simulation of the two experimental campaigns are presented and analyzed.

- **Chapter 6**: In this chapter the summary of the thesis is presented as well as the conclusions obtained from the results. Finally, suggestions for future work are proposed.

Chapter 2. State of the art

This chapter presents the theory behind the principal topics that will be analyzed in detail along the thesis.

The concepts presented in this chapter include:

1. The different **mechanical behavior** of masonry depending on the nature of the stress applied (compression, tension, shear or a combination of them).
2. The **failure criterion** that will be the mathematical basis of the numerical model: the Mohr-Coulomb failure criterion.
3. **Experimental tests** available to characterize the shear mechanical properties of masonry.
4. **Numerical models** used in literature for the analysis of masonry, with their advantages and disadvantages.

2.1 Mechanical behavior of masonry

As explained earlier, masonry is a highly complex material. One of the main problems in characterizing this material arise from the fact that its **mechanical properties depend on the properties of each of the forming materials** (i. e., the mortar and the brick) and the **interaction between them** (Witt, 2014). Besides, this is an **anisotropic** material and the way in which it is constructed (horizontal and vertical joints) have a big impact on its performance. Because of this, the understanding of the mechanical behavior of masonry is so complex.

In this section, the mechanical behavior of masonry is presented to give to the reader an overview of the mechanical concepts that will be treated in detail later in the thesis.

2.1.1 Tensile behavior

Tensile strength usually appears in masonry because of uncentered compressive loads and/or shear loads (Witt, 2014). Since the weakest part of masonry is the interface between brick and mortar, **the tensile strength of masonry is determined by the tensile strength of the joint**.

The characteristic **failure mechanisms**, depending on the type of load, are the followings (Lourenço, 1997):

a) Cracking in the joints (tensile load).

b) Sliding along a bed or head joint (shear load).

c) Cracking of masonry units in direct tension (tensile load).

d) Diagonal tension cracking in units (shear and compression load).

e) Splitting of units (compression load).

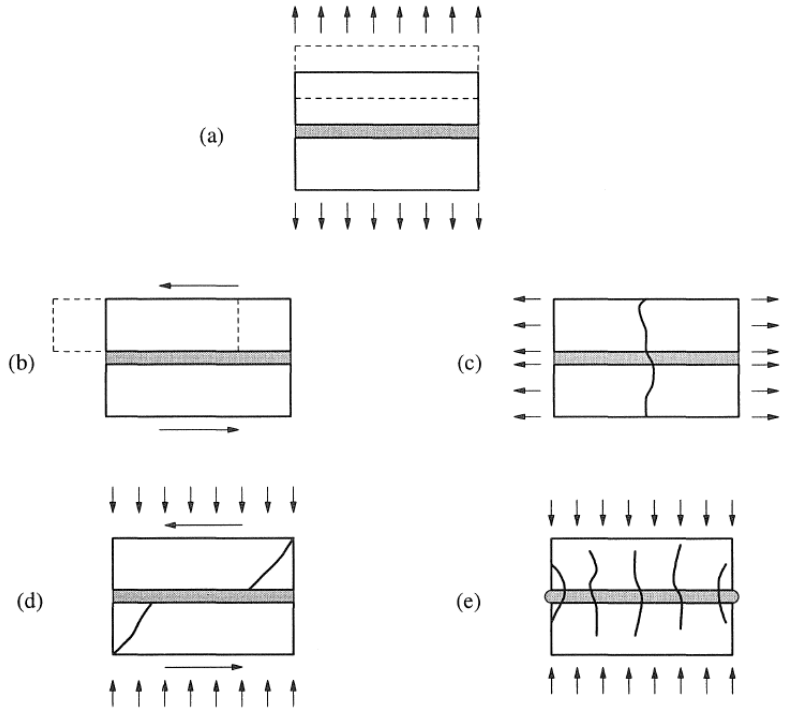

Figure 2. ***Masonry failure mechanisms (Lourenço, 1997).***

It is shown in Figure 2 that for mechanism (a), when the tensile load is applied perpendicular to the joint, the failure is produced by the brick-mortar interface. On the other hand, when the tensile load is applied parallel to the joint (c), the failure is produced in the brick.

The tensile behavior, with respect to the ***stress – displacement*** **diagram**, is characterized by a first **linear elastic** phase that ends when the maximum tensile strength is reached, and **softening** occurs. Softening is defined as the gradual decrease of the resistance under a continuous increase of the deformation.

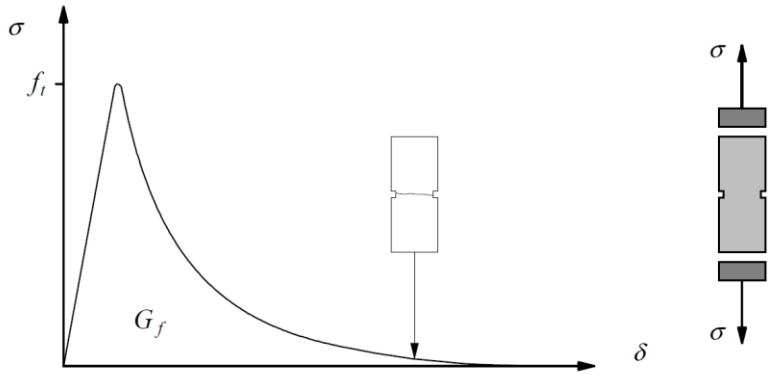

Figure 3. ***Tensile behavior of masonry. Source: (Lourenço, 1996).***

This phenomenon is typical of **quasi-brittle materials** like concrete or masonry, where the material fails because of the successive cracks that appear inside of it.

At the beginning of the loading process, the cracks (which are still "**micro-cracks**") are stable, meaning that only **increase when the load increases**. However, around the maximum tensile strength (f_t), the **macro-cracks** (unstable) appear and the material starts losing **stiffness** (Lourenço, 1996).

Note that the area below the graph corresponds to the tensile fracture energy or **mode-I fracture energy** (G_f^I), which is defined as the **amount of energy needed to break the material** under a tensile stress.

2.1.2 Shear behavior

The shear strength of masonry may be calculated by the cohesive-frictional law provided by the **Mohr-Coulomb** criterion:

$$\tau = c + \sigma tan\phi \qquad \text{Equation 1}$$

where τ stands for the shear stress, c for the cohesion, σ for the normal stress and ϕ for the friction angle. This criterion will be explained in more detail later on.

The shear behavior of masonry with respect to the *stress – displacement* diagram, presented in Figure 4, shows that by **increasing the compression, the shear strength increases**. This fact is because of the **confinement** produced in the brick-mortar interface.

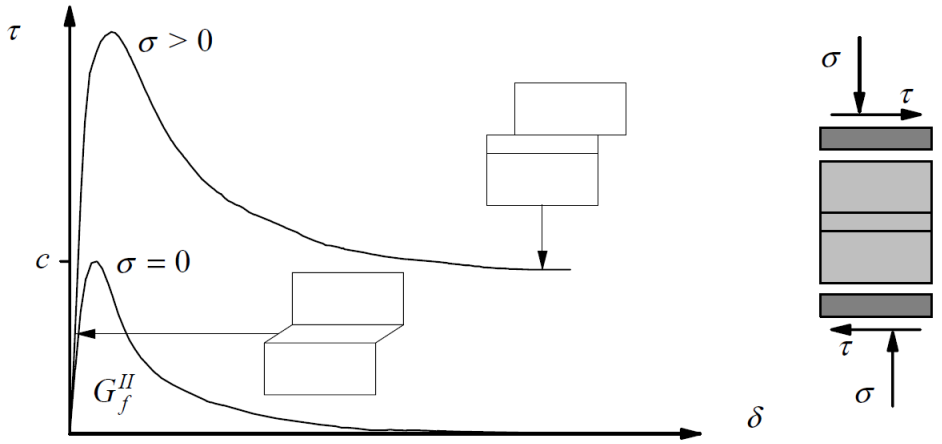

Figure 4. ***Shear behavior of masonry (Lourenço, 1996).***

Again, the diagram has a linear behavior until it reaches the maximum shear strength (if there is no compression, the maximum shear strength corresponds to **cohesion** (c)).

In this case, the energy necessary to break the material is the so-called shear fracture energy or **Mode-II fracture energy** (G_f^{II}). Note that this energy corresponds to the integral of the *shear - displacement* diagram **without normal stress** ($\sigma = 0$), meaning pure shear stress.

2.1.3 Uniaxial compression behavior

The compressive strength depends on many parameters. One of the most important is the **tensile strength of the brick** units (Witt, 2014). The reason for this is that when a perfect compression is applied on masonry, **two tensional states are produced** (see Figure 5):

1. **Brick**: suffers **axial compression and biaxial tension**.
2. **Mortar**: undergoes **triaxial compression**.

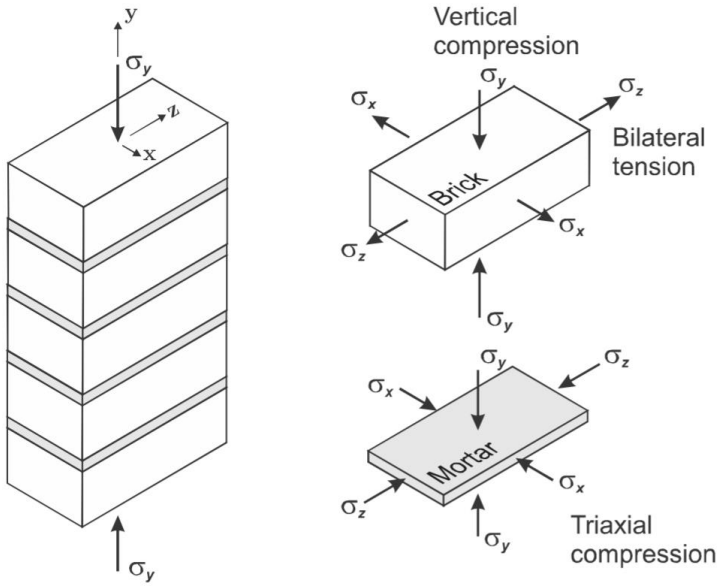

Figure 5. ***Tensional states for pure compression. Source: (Singhal, 2013)***

It was demonstrated in 1969 that the failure of masonry under compression is also due to the **difference between the elastic properties of brick and mortar** (Hilsdorf, 1969). There are two scenarios: the brick is stiffer than the mortar; or the mortar is stiffer than brick. The former is undoubtedly the most frequent case, especially in old buildings. For high strength mortars, the failure is brittle and explosive; for weak mortars, it is soft and slow (Witt, 2014).

Also, the **angle of the joints** has a great impact in the compressive strength and in the failure mechanism. In Figure 6, the failure mechanism depending on the angle formed by the mortar joint and the horizontal axis are presented.

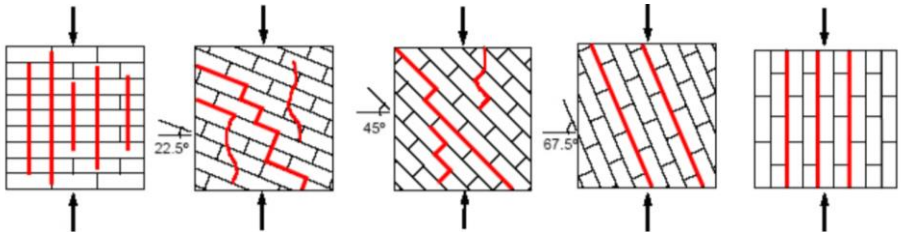

Figure 6. ***Modes of failure of masonry under compression. Fuente: (Page, 1983).***

Note that for the brick-mortar interface, when α is equal to 0º, there is pure compression, when α is equal to 90º, there is pure shear. For angles between these values, there is a combination of these two stress states in the joint.

The compression behavior, with respect to the *stress – displacement* diagram, is characterized by three phases:

1. The first phase is again characterized by a **linear elastic** relationship between stress and displacement.

2. However, when the first micro-crack occurs, the **non-linear** phase begins. During this phase, more load can be applied (unlike the case of traction) and the stiffness is reduced because of the increase of cracks.

3. This situation ends when the micro-cracks become macro-cracks (peak of the curve) and the **softening** begins.

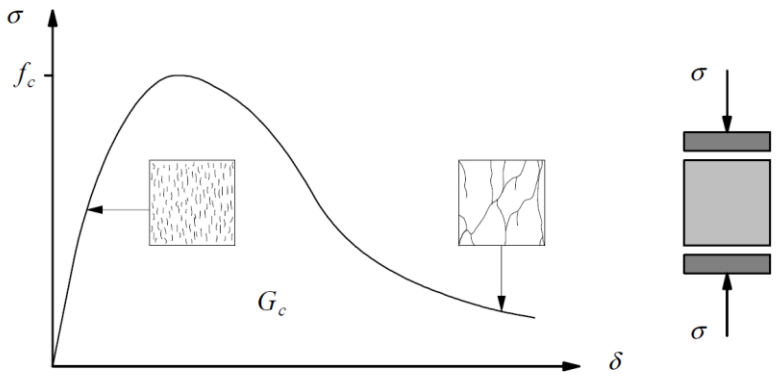

Figure 7. ***Compression behavior of masonry. Source: (Lourenço, 1996).***

2.2 Failure criteria

When materials are subjected to a pure uniaxial stress, like in the cases presented so far, the maximum strength can be determined by the ***stress – displacement* diagram**. However, when a combination of stresses is applied to a material, a failure criterion is needed. Prior to define the failure criteria, there are few concepts that must be introduced.

On the one hand, for any point of a material, the stress tensor (see Figure 8) is defined by 6 components. Depending on the magnitude and the direction of the tensor, three **principal stresses** are obtained: σ_1, σ_2 and σ_3 (such that $\sigma_1 \geq \sigma_2 \geq \sigma_3$).

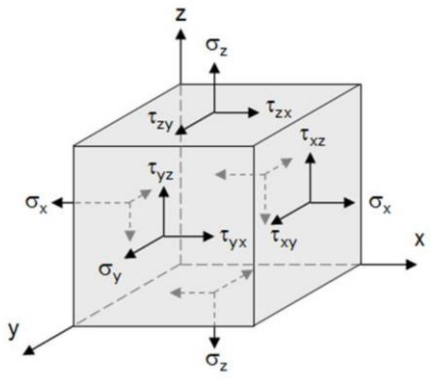

Figure 8. ***Stress tensor (Seller, 2015).***

On the other hand, the **yield surface** is defined as surface such that if the state of stress for a given point is inside, the point is in **elastic regime**. When the stress state touches the boundary of the yield surface, it is said to have reached its yield point and the material becomes inelastic.

The yield surface (f) in 3-D is usually expressed by the three principal stresses. Depending on the definition of the yield surface, different failure criteria are obtained.

$$f(\sigma_1, \sigma_2, \sigma_3) = 0 \qquad \text{Equation 2}$$

Among all the criteria available to define the yield surface, this section provides an explanation of one of the most common ones used in the literature for masonry: the **Mohr-Coulomb failure criteria**. Apart of being one of the most popular, this criterion is **used as a basis to define the material model** used in the simulations presented in section 4 of this document. Therefore, its presentation is useful.

2.2.1 Mohr-Coulomb failure criterion

The Mohr–Coulomb failure criterion is defined by a set of linear equations in principal stress space that describes the **conditions for which an isotropic**

material fails. The effect of the intermediate principal stress σ_2 is neglected. This criterion may be written as a function of the normal stress σ and shear stress τ.

Coulomb established the relation already presented in equation 1 in this document ($\tau = c + \sigma tan\phi$). The representation of this equation in the Mohr diagram corresponds to Figure 9:

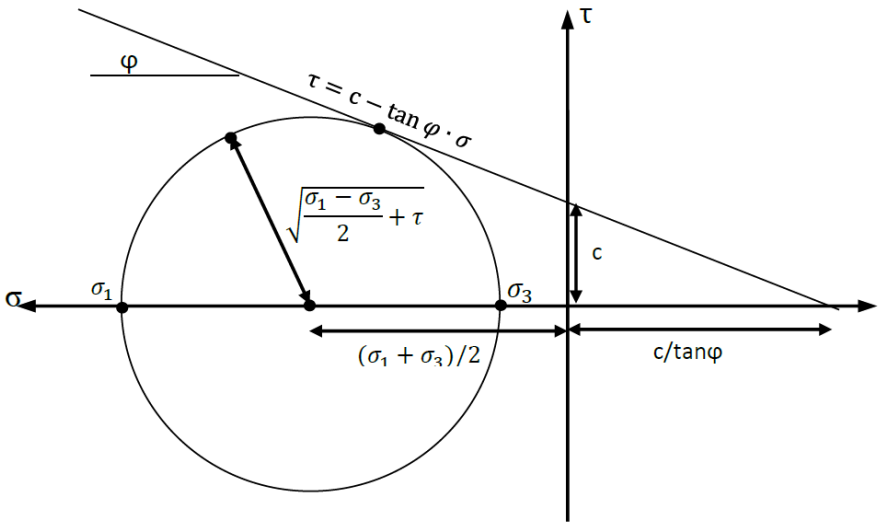

Figure 9. ***Mohr-Coulomb diagram and failure envelope (Witt, 2014).***

Defining σ_t as the tensile stress and σ_c as the compression one, the following equations may be obtained by trigonometric relations:

$$\sigma_t = \frac{2 \times c \times \cos(\varphi)}{1 + \sin(\varphi)} \qquad \text{Equation 3}$$

$$\sigma_c = \frac{2 \times c \times \cos(\varphi)}{1 - \sin(\varphi)} \qquad \text{Equation 4}$$

Making use of the circles and the Mohr-Coulomb failure criterion, it can be predicted if a part of **the material fails if the envelope** formed by the Mohr circles in uniaxial tension and in uniaxial compression respectively **is crossed**.

This model is widely used to estimate the compressive and tensile strength with the data obtained in experimental campaigns.

2.3 Experimental tests for masonry

In order to understand the behavior of masonry and to obtain its mechanical parameters, it is necessary to carry out **experimental tests**. However, standard tests considered in regulations are hardly applicable to existing structures since they require the extraction of big samples (Marastoni, et al., 2016).

A relatively novel approach is the use of **MDT** (Minor Destructive Testing) procedures that are based on an **in-situ sampling of small diameter cores** that can be later tested in the laboratory (Pelà, et al., 2017). This procedure is more appropriate for historical structures, since it allows to take small samples from “hidden” elements of the original structure to maintain its integrity and aesthetics.

The specimens that are extracted from existing structures to be tested in the laboratory are usually small; the classic diameters are **70 mm** or **110 mm** (Pelà, et al., 2017). This is fundamentally due to two reasons:

1. In existing structures, the impact of the sample extraction must be as low as possible, especially when these structures have an **historical value**. It is not possible to extract big samples such as walls, for instance, in historical cathedrals or monuments.

2. If tests are performed in big samples, such as walls, the resistance obtained may be much lower than the real ones. The reason for this is that the extracted wall is **microcracked in the transport and handling to the laboratory**. Therefore, the resistance obtained will be lower because of this damage. On the other hand, if a small cylindrical test is extracted, it can be confined so it maintains its mechanical properties until reaching the laboratory, obtaining a more realistic result on the tests.

Finally, experimental tests applied to small masonry sections or specimens to determine its shear strength of the mortar joint are presented. By using these tests, different parameters may be obtained to be used as the **input for numerical models**: cohesion, friction angle, dilatancy angle, etc.

2.3.1 ASTM C1531

This test is used in situ and following the American code (ASTM C1531) is able to provide the qualitative shear strength index for mortar joints. This parameter is calculated using both the data provided by experiments and calculations. According to the ASTM C1531, it is advised to use this test away from openings or well ends.

2.3.2 Couplet Test

The main advantage of the Couplet test is the simplicity in the way that it is applied. According to Figure 10, two vertical compressive loads F_{n1} and F_{n1} are applied on the top horizontal steel beam to distribute the load on the specimen below it, and balance the moment induced by the shear load. The specimen is formed by two bricks bonded with a single mortar joint.

To obtain good results, the specimen must be properly fixed to guarantee that the shear force acts on the plane of the joint (Hendry, 1990).

The vertical load is applied slowly until a certain value is reached. From this moment on, the load is kept constant until the end of the test. At the same time, a horizontal load F_s is applied to introduce shear stress in the joint.

The loads are measured with a load cell and the displacements are measured with LVDTs (linear variable differential transformers).

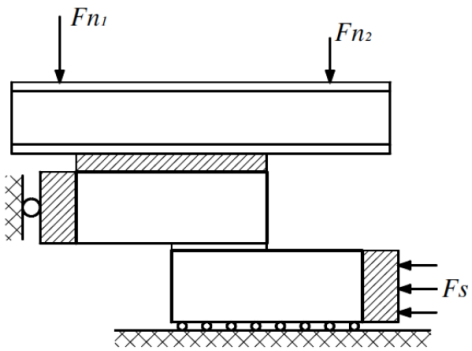

Figure 10. ***Couple test (Lourenço, et al., 2004).***

2.3.3 Triplet Test

Making honor to name of the test, three bricks are used in this experimental test. The problem of this test comes with the introduction of bending effects, that must be minimized by properly fixing the specimen (Lourenço, et al., 2004).The normal compressive stress is slowly loaded like in the case of the Couplet test. Again, once a certain value of load is reached, the value is kept constant during the rest of the test. The displacements are also measured through the use of LVDTs and loads, with load cells.

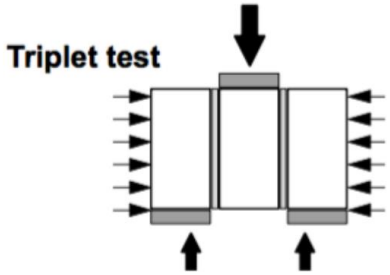

Figure 11. *Triplet test (Lourenço, et al., 2004).*

2.3.4 Van der Pluijm Test

In the Van der Plujim test, two masonry units joint with mortar are placed inside two steel molds. The purpose of the steel molds is to distribute the horizontal loads as well as the vertical. This test avoids bending, since the shear stress is applied directly on the joint.

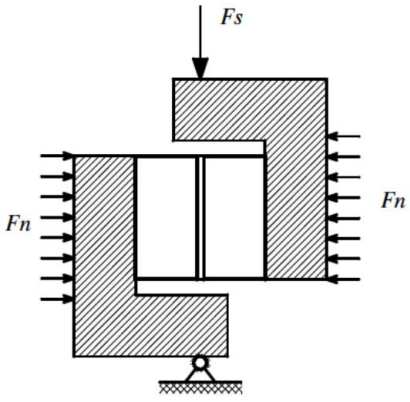

Figure 12. *Van der Plujim test (Lourenço, et al., 2004).*

2.3.5 Brazilian Test

In the experimental campaigns presented in the following chapter of the thesis, the approach selected to obtain the shear behavior in masonry was the **Brazilian test**. In this test, the applied force is split into a tangential and a normal force, therefore, the joint will have a compression and shear state.

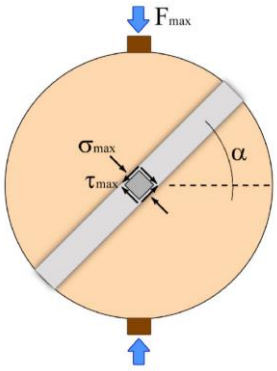

Figure 13. ***Scheme of the forces in a Brazilian test (Marastoni, et al., 2016).***

The equations used to transform the vertical load into the shear and normal stresses on the brick-mortar interface are the following ones:

$$\sigma_{max} = \frac{F_{max}}{A}\cos\alpha \qquad \text{Equation 5}$$

$$\tau_{max} = \frac{F_{max}}{A}\sin\alpha \qquad \text{Equation 6}$$

where the area (A) corresponds to the section of the interface (i. e., the product of the diameter times the length of the core sample).

Depending on the angle α formed by the mortar joint and the horizontal axis, the magnitude of the shear and compression forces that act on the brick-mortar interface vary: **the greater angle α, the greater shear and lower compression**; the lower α, the greater compression and lower shear.

2.4 Numerical models for masonry

Since experimental tests are very expensive, it is very important to perform numerical simulations. A novel practice in research is to com**bine a few experimental tests with numerical models**.

The main advantages of numerical simulations with respect to laboratory experiments are:

- The **economical cost** is drastically reduced.
- A **large number of tests** (simulations) can be performed.
- It allows the **visualization** of the results (post-process).

The disadvantages, or needs, are:

- It may require a big **computational power**.
- It may not be trivial to determine whether the results obtained are correct or not during the **calibration** process.

As it was said earlier, the elements that compose the masonry have very **different elastic and inelastic properties**. In addition, variations in the position of these elements leads to **different failure mechanisms** (Petracca, et al., 2017). Several computational strategies exist in the literature to deal with the numerical analysis of such a complex material (Roca, et al., 2010):

- **Macromodel**: the entire structure is modeled as a single element. It is the most simplified model. It is used to model buildings in practice, but the results do not allow us to interpret the results well. In research it is not used.

- **Simplified micromodel**: the brick is represented as a continuous element and the mortar joint as an interface.

- **Detailed micromodel**: the brick is represented as a continuous element and is joined as another continuous element, plus a discontinuous interface. With this option the most accurate results are obtained, although the computational cost is higher (and the time required).

The following figure shows the elements of each modelling strategy:

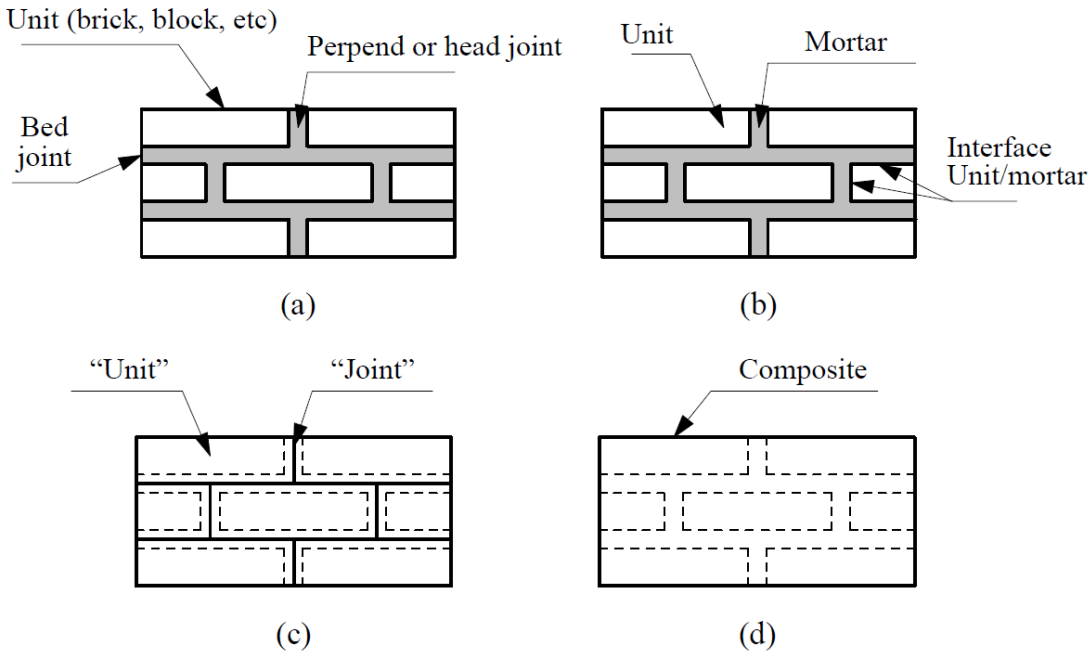

Figure 14. ***Modeling strategies: a) masonry sample, b) detailed micromodel, c) simplified micromodel, d) micromodel (Lourenço, 1997).***

2.4.1 Macromodels

Macromodels, also known as continuous models, make **no distinction between the various elements** that make up the structure as a whole.

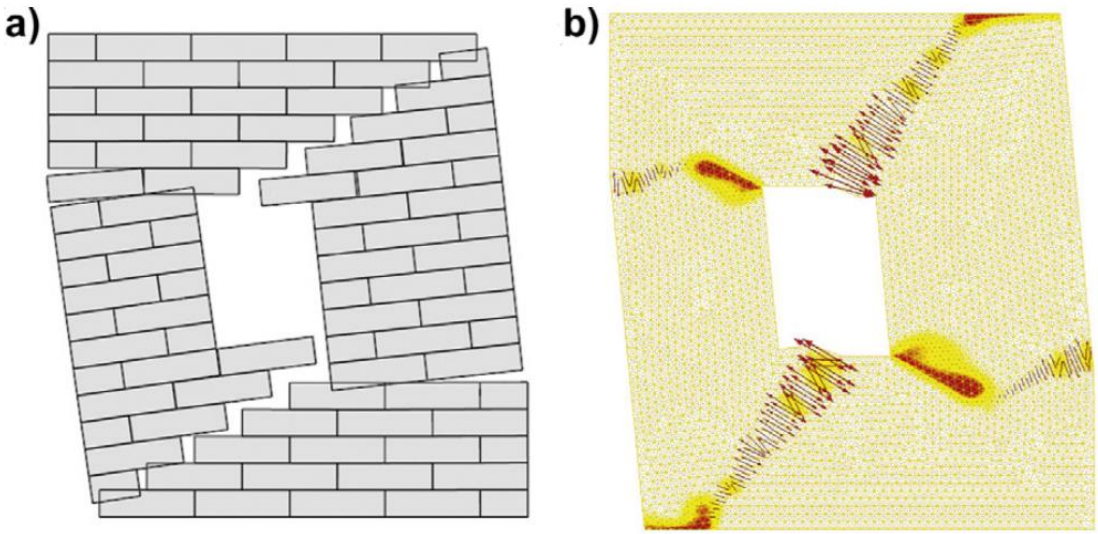

Figure 15. ***Comparison between a micromodel of a wall a) and a macromodel b) (Pelà, et al., 2012).***

The main difficulty in implementing this model lies in (Petracca, et al., 2017):

1. It is necessary to choose **mechanical parameters that represent all the elements of the material**. For instance, it is necessary to choose a compressive strength representative both for the brick and the mortar. This is unreal since the different elements have very different mechanical characteristics.

2. Define **realistic failure phenomena**. If the model is defined as a whole, it cannot take into account the weak points of the structure, i. e. the joints. Therefore, the cracking pattern may not be realistic at all.

However, macromodels are the most widespread option in the numerical analysis of **large structures** due to their low computational cost.

2.4.2 Micromodels

If it is intended to make a detailed description of the microstructure of masonry, more detailed models are needed. Moreover, since masonry is subjected to a **triaxial state of stresses**, it is necessary to use three-dimensional models to capture all the phenomena that occurs inside it. However, this entails **high computational costs**.

In specific cases, the assumption of **2-D** can be taken, which greatly simplifies the problem. However, this can lead to inaccurate results when masonry is subjected to very high compressions, since the triaxial compression state in the mortar joints cannot be represented with the plane stress assumption (Petracca, et al., 2017).

In summary, **micromodels are used in relatively small structures** in which the interaction between brick and mortar is of special interest (research field). On the contrary, **for larger structures**, the memory and the time required for the use of micromodels is prohibitive and **macromodels** are used (industry field).

Chapter 3. Reference experimental campaigns

As explained in the goals of the thesis, in order to understand the mechanical behavior of the interface joint of masonry, a numerical model is needed. In this study, the model must be able to replicate the results obtained in experimental campaigns carried out by two groups of investigators: Marastoni, et al., 2016 and Pelà, et al., 2017.

3.1 Experimental campaign by Marastoni et al. (2016)

In 2016, a group of investigators from the Universitat Politècnica de Catalunya and the University of Bologna, published the paper "*Combining Brazilian tests on masonry cores and double punch tests for the mechanical characterization of historical mortars*" (Marastoni, et al., 2016).

In this paper, the researchers presented the results of an experimental campaign that was carried out in the Laboratory of Technology of Structures and Materials of the Technical University of Catalonia (UPC - Barcelona Tech) in 2015.

In this study, two different tests were performed to characterize **historical mortars**: **Double Punch Test** (DPT) and **Brazilian Test**. The latter is the one of interest for this thesis, which allows to apply shear loads on cylindrical masonry specimens with different angles to obtain different states of stress. The specimens tested, had one diametral mortar joint.

In their study, once the samples were obtained, two models were used to estimate the mechanical properties of the mortar interface: a *Continuum Model* and an *Interface Model*. The former is filled with the DPT and the Brazilian Tests samples, while the latter is filled only with the Brazilian Test results.

The experimental tests were carried out on specimens that recreated the materials used in historical masonry, with **low mechanical properties**: the manufacture and curing of the mortar was carefully executed using traditional techniques in the laboratory.

Once the materials were selected, two walls were built up with dimensions $1{,}6 \times 0{,}8 \times 0{,}145\ m^3$. The external mortar joints had a thickness between 15 and 20 mm.

After 60 days of curing, the horizontal core drilling was executed perpendicularly to the face of the walls using a novel dry extraction procedure that allowed to preserve the integrity of the joints by using air cooling instead of water cooling. With this procedure, 22 samples of 90 mm of diameter were obtained.

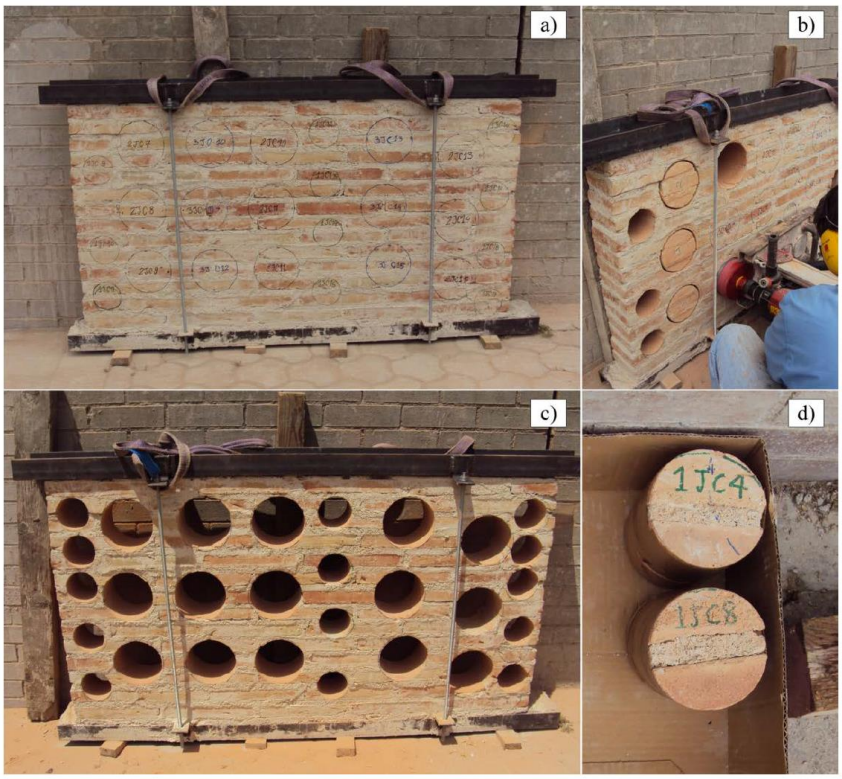

Figure 16. ***Masonry walls a), masonry walls during extraction b), masonry walls after extraction c) and samples extracted d).***

The samples extracted were subjected to Brazilian tests 210 days after the extraction. A compression machine with vertical displacement control was used to test the samples with different angles: **45º, 50º, 55º and 60º**. A wooden strip was used to distribute the force applied in the top of the specimen.

The next figure shows the results obtained for the four different angles. Note that the joint relative displacement (horizontal axis in Figure 17) corresponds to the relative sliding displacement of the joints.

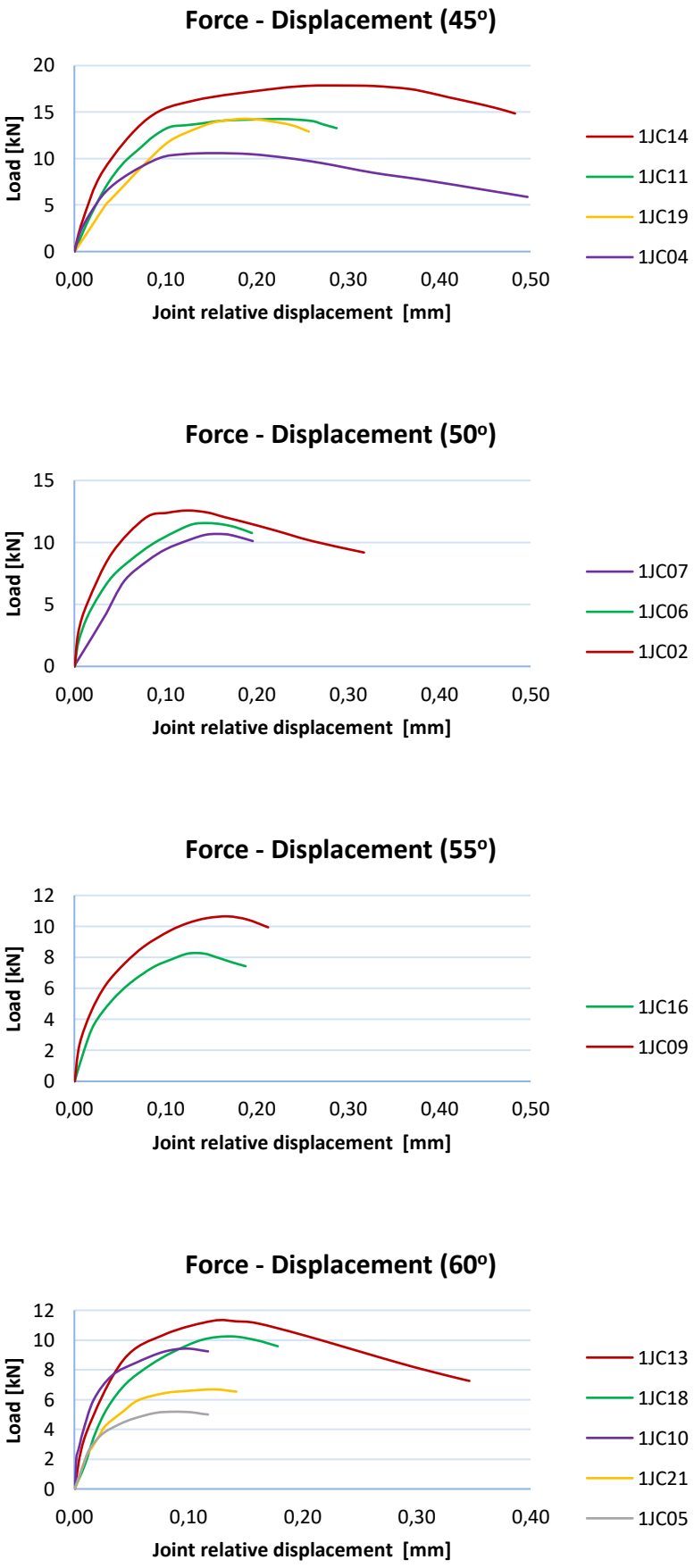

Figure 17. *Load – Joint Relative Displacement for α=45º, α=50º, α=55º and α=60º.*

Once the diagrams are obtained, the normal and shear stresses can be obtained using equations (5) and (6) presented before.

Sample	***α [°]***	***F_{max} [kN]***	***σ_{max} [MPa]***	***τ_{max} [MPa]***
1JC04	45	10,62	0,56	0,56
1JC11	45	14,19	0,76	0,76
1JC14	45	17,87	0,95	0,95
1JC19	45	14,26	0,76	0,76
1JC02	50	12,50	0,58	0,69
1JC06	50	11,53	0,55	0,66
1JC07	50	10,68	0,52	0,61
1JC09	55	10,63	0,46	0,66
1JC16	55	8,25	0,36	0,51
1JC05	60	5,12	0,19	0,33
1JC10	60	9,39	0,35	0,61
1JC13	60	11,32	0,42	0,73
1JC18	60	10,20	0,39	0,67
1JC21	60	6,69	0,26	0,45
Avg 45°	**45**	**14,23**	**0,76**	**0,76**
CV% 45°		21%	21%	21%
Avg 50°	**50**	**11,57**	**0,55**	**0,66**
CV% 50°		8%	6%	6%
Avg 55°	**55**	**9,44**	**0,41**	**0,58**
CV% 55°		18%	18%	18%
Avg 60°	**60**	**8,54**	**0,32**	**0,56**
CV% 60°		30%	30%	30%

Table 1. Results of the experimental campaign.

From the results presented in the table before, an *Interface Model* was used in the paper of Marastoni et al.: the mortar joint is considered as a zero-thickness interface between the two halves of the specimen.

It must be noted that **the Interface Model**, is a simplification that **does not account for the triaxial stress in the joint**, and only considers the shear and the normal stress. In this model, the failure of the mortar consists on the sliding of the joint.

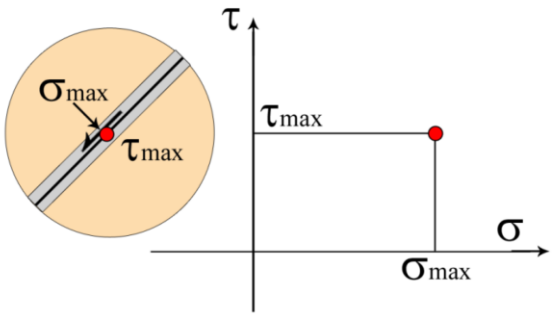

Figure 18. *Interface model scheme (Marastoni, et al., 2016).*

The failure envelope of the model is then obtained by linear regression of the data provided in Table 1 which yields to a Mohr-Coulomb criterion characterized by a **friction angle $\phi = 32,32^{o}$ and cohesion $c = 0,32\ MPa$**.

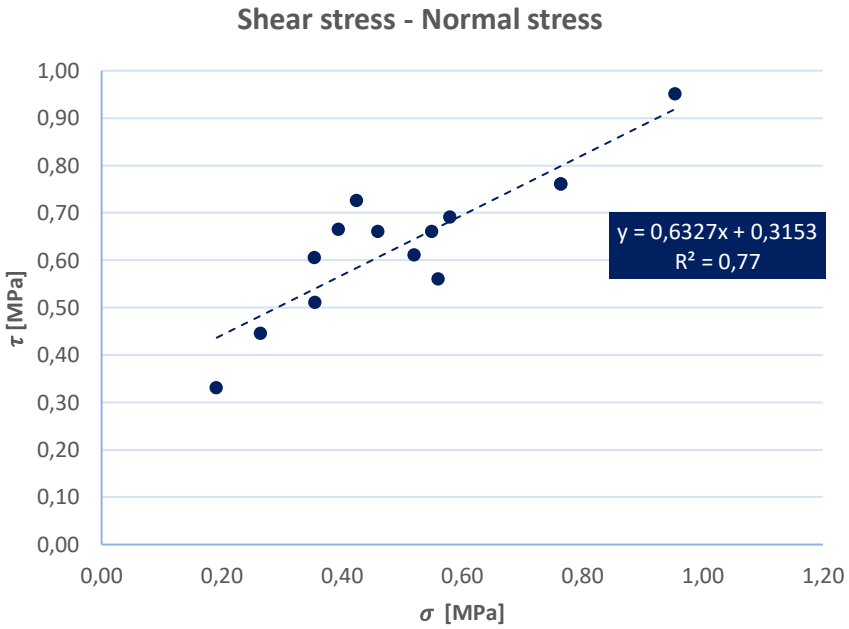

Figure 19. *Estimated linear Mohr-Coulomb regression. Source: (Marastoni, et al., 2016).*

Note that the coefficient of determination was $R^2 = 0{,}77$, meaning a **considerable scattering** in the Brazilian tests.

The *Interface Model* does not allow to calculate neither the maximum mortar tensile strength nor the compression one. Therefore, in the study of Marastoni et al. (2016), the *Continuum Model* was used to estimate its values.

According to the *Continuum Model*, the state of stress in the mortar joint can be represented in the σ - τ Mohr's plane using Mohr's circles. The circles representing the mortar's stress state at failure are tangent to the failure envelope: the Mohr-Coulomb criterion represented by a straight line.

However, in the study of Marastoni et al. (2016), a novel improvement of the *Continuum Model* was presented with the adoption of a Mohr's parabolic failure criterion that was adjusted with the least squares method applied to the Mohr's circles obtained from the Brazilian Tests and the DPTs.

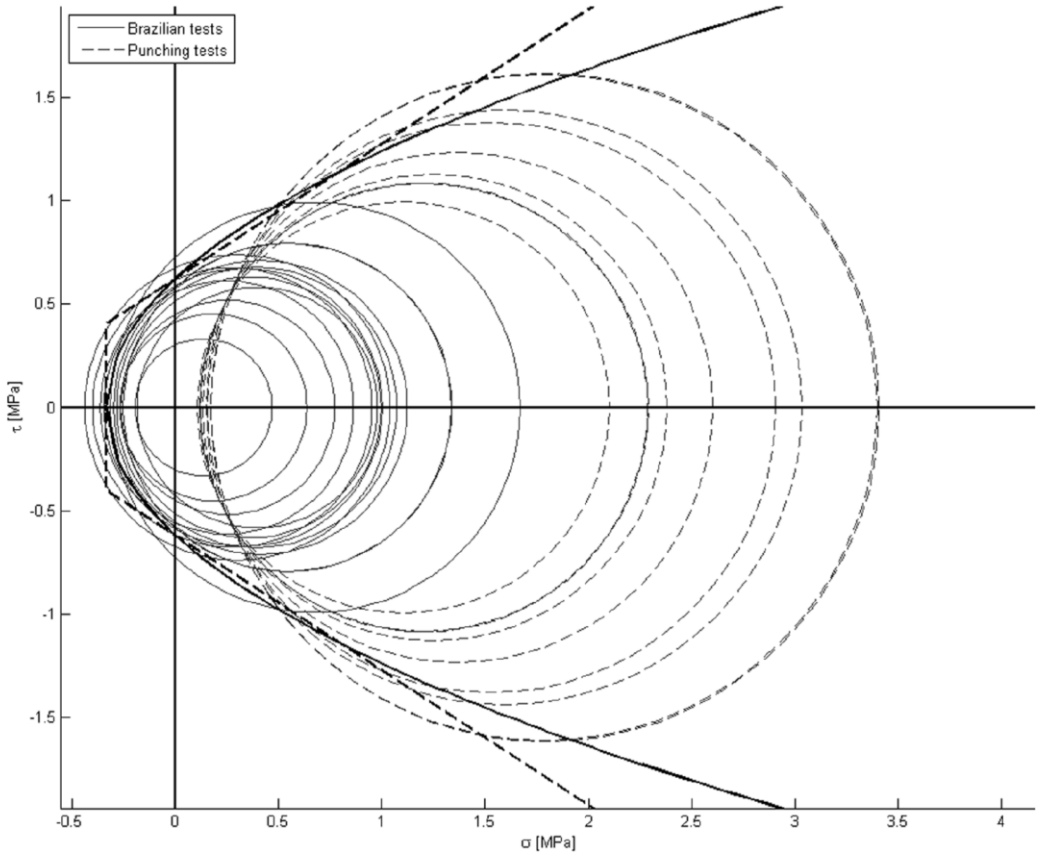

Figure 20. ***Estimated parabolic and linear Mohr-Coulomb domains obtained from DPTs and BTs (Marastoni, et al., 2016).***

The *Continuum Model* provided a **mortar tensile strength of 0,35 MPa and a mortar compressive strength of 2,32 MPa**.

Finally, the mechanical properties of the brick and the mortar measured or estimated in the study, are summarized in the following table:

Symbol	Parameter	Value	Units
f_{cm}	Compression strength mortar	2,32	MPa
f_{tm}	Tensile strength mortar	0,35	MPa
c	Cohesion	0,32	MPa
ϕ	Friction angle	32,32	º
h_m	Joint thickness	15	mm
h_u	Unit thickness	77	mm
E_u	Young Modulus brick	9792	MPa
E_m	Young Modulus mortar	400	MPa
G_m	Mortar shear elastic modulus	154	MPa
f_{cu}	Compression strength unit	18,40	MPa
f_{tu}	Tensile strength unit	3,63	MPa
k_h	Confinement ratio	0,42	-
v_m	Poisson mortar	0,30	-
v_u	Poisson unit	0,17	-

Table 2. Mechanical properties of bricks and mortar. Source: (Marastoni, et al., 2016).

3.2 Experimental campaign by Pelà et al. (2017)

In 2017, a group of investigators from the Universitat Politècnica de Catalunya published the paper "*Experimental evaluation of the shear strength of aerial lime mortar brickwork by standard tests on triplets and non-standard tests on core samples*" (Pelà, et al., 2017).

In this paper, the researchers presented the results of an experimental campaign that was carried out in the Laboratory of Technology of Structures and Materials of the Technical University of Catalonia (UPC - Barcelona Tech).

The purpose of the study was to evaluate the **shear response of aerial lime mortar masonry**. Two different tests were carried out: standard **shear tests** on masonry triplets and **Brazilian tests** on cylindrical specimens with different inclinations of the mortar joint. The specimens had also one diametral mortar joint.

The experimental tests were carried out on specimens that recreated the materials used in historical masonry, with **low mechanical properties**, i. e. solid clay bricks and lime mortar joints.

Two walls were constructed with dimensions $1{,}605 \times 0{,}870 \times 0{,}145\ m^3$. After one year from its construction, the horizontal core drilling was executed perpendicularly to the face of the walls using a dry extraction procedure that allowed to minimize the risk of disjointing the cylindrical specimens. With this procedure, **15 undamaged samples of 90 mm of diameter** were obtained to carry out the Brazilian test.

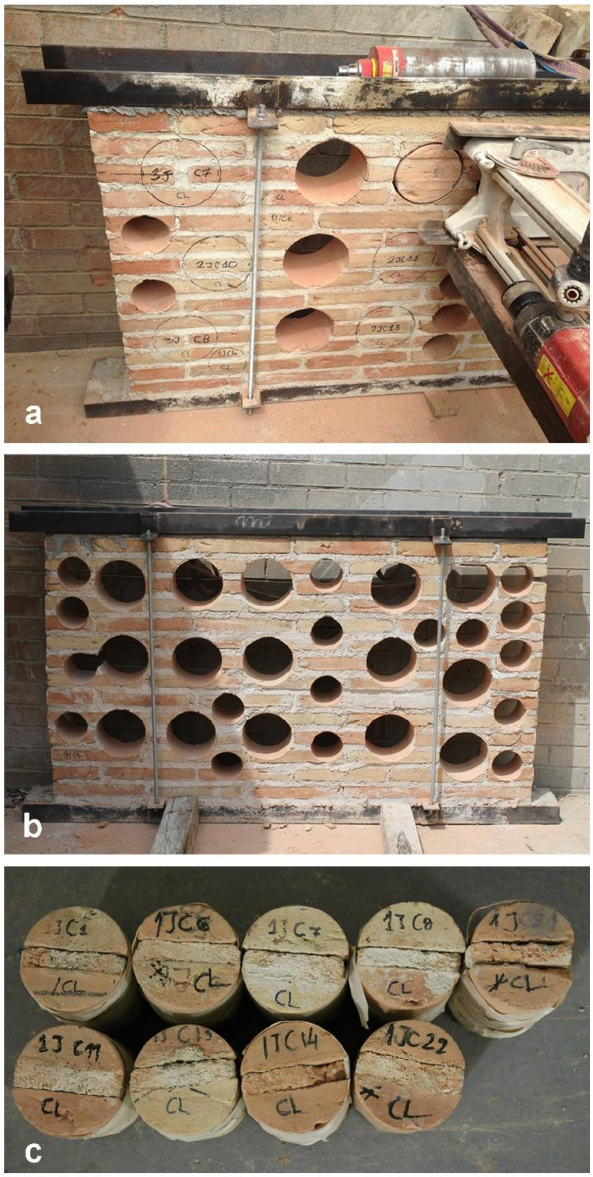

Figure 21. ***a) Masonry walls during extraction, b) masonry walls after extraction and c) samples extracted.***

A compression machine with vertical displacement control was used to test the samples with different angles: **40º, 45º and 50º**. A wooden strip was used to distribute the diametric longitude load on the top of the specimen.

Next table shows the results obtained for the three different angles. The joint relative displacement corresponds to the sliding displacement of the joint:

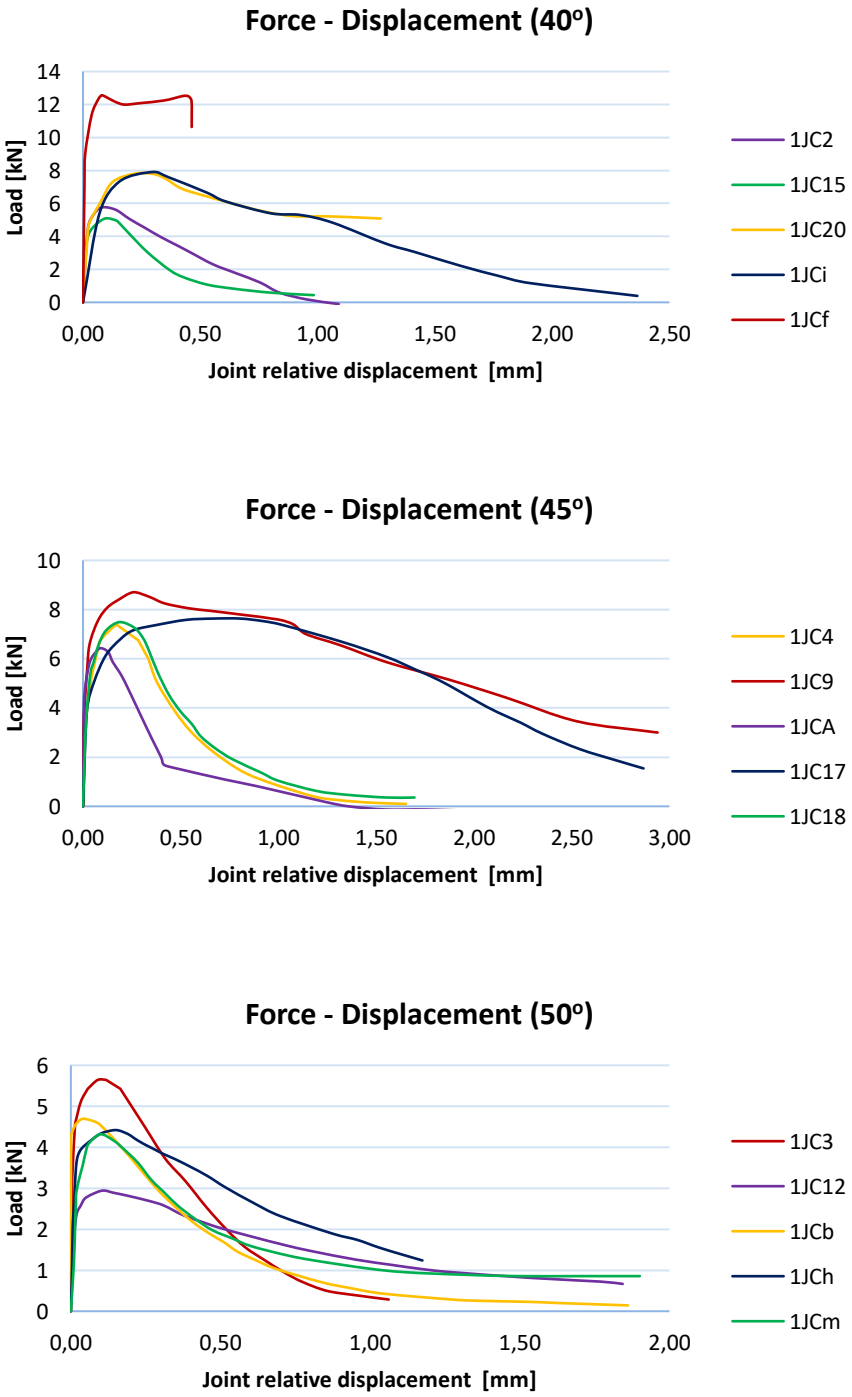

Figure 22. ***Load – Joint Relative Displacement for 40º, 45º and 50º.***

Once the diagrams are obtained, the normal and shear stresses are again calculated using equations (5) and (6).

Sample	***α [°]***	***F_{max} [kN]***	***σ_{max} [MPa]***	***τ_{max} [MPa]***
C2	40	5,699	0,335	0,281
C15	40	5,138	0,302	0,253
C20	40	7,925	0,465	0,390
Ci	40	7,889	0,463	0,389
Cf	40	12,79	0,750	0,630
C4	45	7,334	0,397	0,397
C9	45	8,893	0,482	0,482
C17	45	7,696	0,417	0,417
C18	45	7,424	0,402	0,402
CA	45	6,449	0,349	0,349
C3	50	5,746	0,283	0,337
C12	50	2,957	0,146	0,174
Cb	50	4,73	0,233	0,278
Ch	50	4,436	0,218	0,260
Cm	50	4,324	0,213	0,254
Avg 45°	**40**	**7,887**	**0,463**	**0,388**
CV% 45°		34%		
Avg 45°	**45**	**7,559**	**0,410**	**0,410**
CV% 45°		10%		
Avg 50°	**50**	**4,439**	**0,212**	**0,261**
CV% 50°		20%		

Table 3. Results of the experimental campaign (Pelà, et al., 2017).

From the results presented in the table before, the same *Interface Model* described in Marastoni et al. (2016) was used to estimate the cohesion and friction angle: the failure envelope of the model is obtained by linear regression and yields to a Mohr Coulomb criterion characterized by a **friction angle $\boldsymbol{\phi = 35,86^o}$ and cohesion $\boldsymbol{c = 0,09\ MPa}$**.

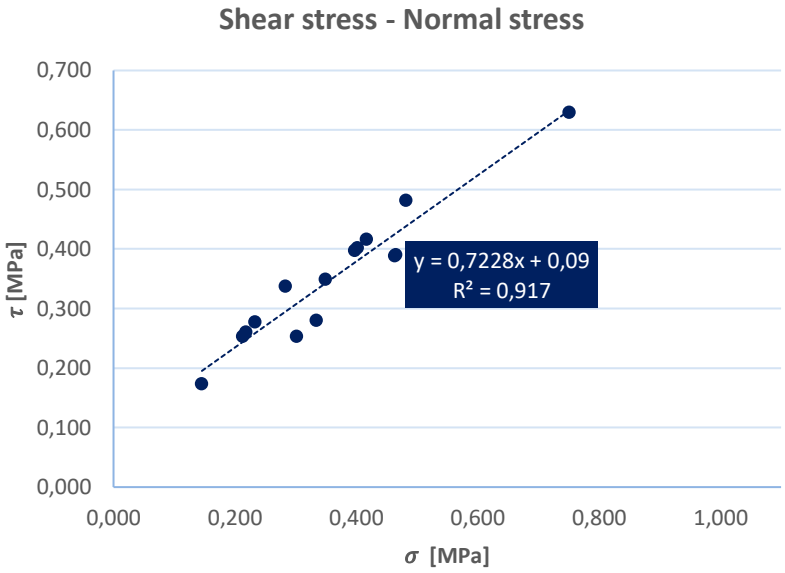

Figure 23. ***Estimated linear Mohr-Coulomb domain. Source:***

In this case, the coefficient of determination is $R^2 = 0{,}92$, providing a **good correlation** for the interpolation of the experimental data.

Again, the *Continuum Model* was used to estimate the mortar tensile strength and the compression strength. Finally, all the mechanical properties of the brick and the mortar obtained in this study, are summarized in the following table:

Symbol	**Parameter**	**Value**	**Units**
f_{cm}	Compression strength mortar	1,02	MPa
f_{tm}	Tensile strength mortar	0,39	MPa
c	Cohesion	0,09	MPa
ϕ	Friction angle	35,86	º
h_m	Joint thickness	17	mm

Table 4. Mechanical properties of bricks and mortar (Pelà, et al., 2017).

Chapter 4. Numerical micro-model

As said before, the starting point of this thesis is the development of a numerical model. This model is created with the finite element software **DIANA-FEA** (*Displacement Analyzer - Finite Element Analysis*), widely used by masonry researchers. This software provides **constitutive laws designed to simulate the mortar-brick interface**.

The brick-mortar interface is of vital importance in shear tests. The interface allows discontinuities in the displacement field. In addition, it acts as a plane of weakness and is the main responsible for inelastic behavior (Lourenço, 1996). For this reason, a correct modeling of this element is necessary.

In the model presented in this work, the **brick units** are modeled as **continuum linear elastic elements** while the **mortar joints** are modeled with **interface elements**, which obey the nonlinear behavior described by this combined cracking-shearing-crushing model.

4.1 Combined Cracking-Shearing-Crushing model (CSC)

The nonlinear behavior of the interface elements has been modeled with DIANA FEA software. This finite element software provides an interface material model that allows to simulate fractures, frictional slips and crushing along mortar interfaces in masonry (DIANA, 2017).

This model, known as ***Combined Cracking-Shearing-Crushing model*** (CSC), is a plasticity based multi-surface interface model based on the theory of Lourenço and Roots (Lourenço & Rots, 1997).

The CSC model is defined as “multi-surface” since it is composed by the fluence area limited by 3 criteria (see Figure 24):

- **Criterion 1: Cut-off tension.**
- **Criterion 2: Coulomb friction model.**
- **Criterion 3: Compression cap model.**

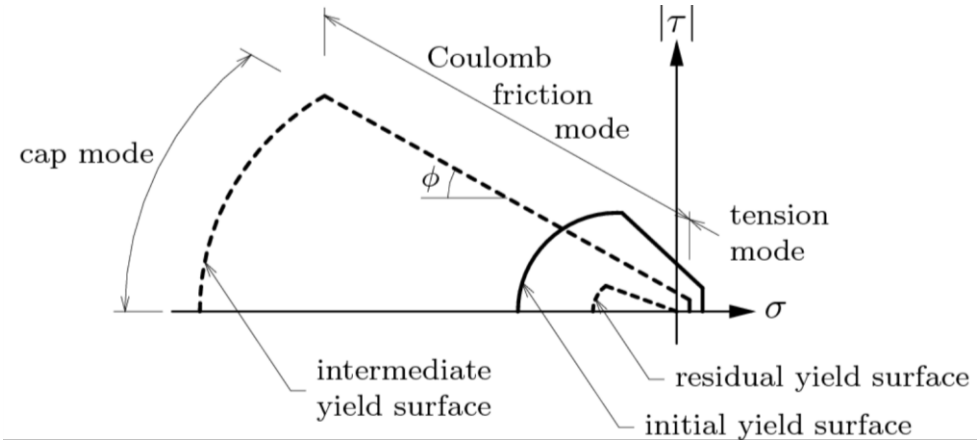

Figure 24. ***CSC model (DIANA, 2017).***

4.1.1 Criterion 1: Tension cut-off

The first criterion (f_1) of the interface model describes the cracking of the interface. This criterion **limits the tensile stresses** that can occur at the interface and is established by the value of the tensile strength of the joint, f_t, and the Mode-I fracture energy (G_f^I). This criterion is calculated using the tensile strength (σ_t) by means of the following equation:

$$f_1 = \sigma - \sigma_t \qquad \text{Equation 7}$$

The tensile strength is exponentially smoothed with respect to its value, the value of the plastic strain k_1 and Mode-I fracture energy (DIANA, 2017):

$$\sigma_t = f_t e^{\left(-\frac{f_t}{G_f^I} k_1\right)} \qquad \text{Equation 8}$$

These parameters depend on the properties of the units, the mortar and the stresses. Fracture energy is defined as the area below the Mode-I diagram, as shown in the following figure:

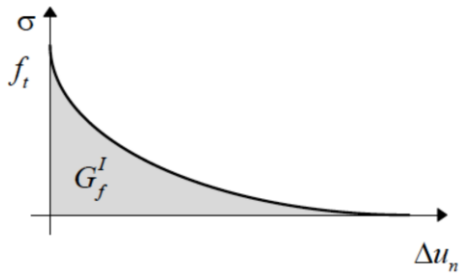

Figure 25. ***Mode-I fracture energy (G_f^I) (Lourenço, 1997).***

4.1.2 Criterion 2: Coulomb friction model

The second criterion of the model is related to the slippage of the interface. This criterion **limits the normal and tangent tensions** according to the **Coulomb friction criterion** by means of the following equation:

$$f_2 = |\tau| + tan\Phi\, \sigma - c \qquad \text{Equation 9}$$

This equation depends on the friction angle ϕ and the cohesion (c). The softening of the cohesion is described by means of its initial cohesion (c_o) y and the Mode-II fracture energy (G_f^{II}) (DIANA, 2017):

$$c = c_o e^{\left(-\frac{c_0}{G_f^{II}} k_2\right)} \qquad \text{Equation 10}$$

The friction softening is coupled to the adhesion softening via:

$$\Phi = \Phi_0 + (\Phi_r - \Phi_0)\frac{c_o - c}{c_o} \qquad \text{Equation 11}$$

where Φ_0 y Φ_r correspond to the initial and the residual friction angles, respectively.

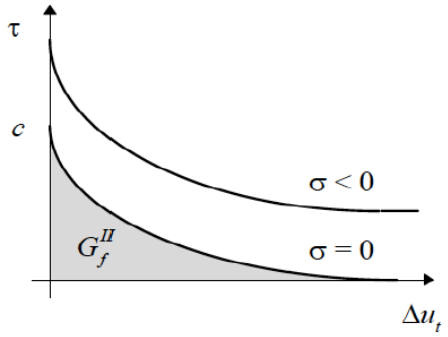

Figure 26. ***Mode-II fracture energy (Lourenço, 1997).***

4.1.3 Criterion 3: Compression cap model

The third criterion of the interphase model is related to the compression limit that describes the crushing of the interface. The compressive inelastic law is defined by the two values of compression fracture energy G_c and the relative equivalent plastic displacement κ_p (Lourenço, 1997). The compression limit criterion is calculated using the compressive strength (σ_c) and the shear-tensile contribution factor (c_s):

$$f_3 = \sigma^2 + c_s\tau^2 - {\sigma_c}^2 \qquad \text{Equation 12}$$

Compression strength (σ_c) increases according to the strain hardening hypothesis (see Figure 27). The parabolic hardening rule specifies that initially the yield surface will suffer hardening. It would then be followed by parabolic softening until it reaches a peak strength f_c. This peak is reached at the plastic strain κ_p this point the softening branch begins and it is governed by the compressive fracture energy G_c (DIANA, 2017).

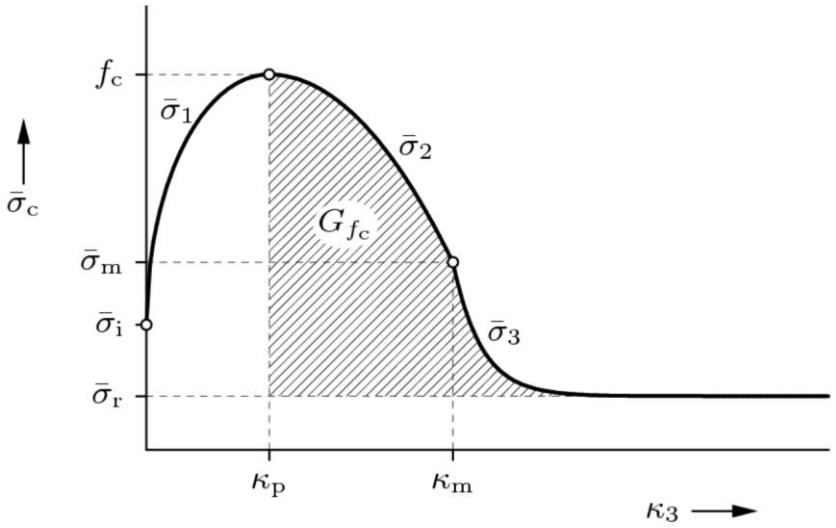

Figure 27. ***Hardening-softening law for compression cap (DIANA, 2017).***

4.1.4 Interface elements

The interface elements stablish the relation between the forces on the interface and the displacements on the two sides of the it. This relation is obtained with the following equation:

$$\sigma = \mathrm{D}\,\varepsilon \qquad \text{Equation 13}$$

The model stablishes a relation between traction and the relative displacement along the interface (Lourenço, 1996). The interface element's traction vector is defined by its normal t_n and shear t_t traction:

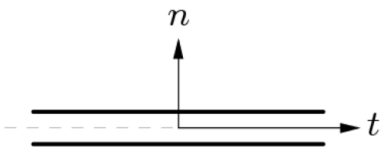

Figure 28. ***2-D Interface element (DIANA, 2017).***

$$t = \begin{Bmatrix} t_n \\ t_t \end{Bmatrix} \qquad \text{Equation 14}$$

Whereas, the relative displacement is defined as:

$$\Delta u = \begin{Bmatrix} \Delta u_n \\ \Delta u_t \end{Bmatrix} \quad \text{Equation 15}$$

The relation between traction and displacement is defined as:

$$\begin{Bmatrix} t_n \\ t_t \end{Bmatrix} = \begin{bmatrix} K_n & 0 \\ 0 & K_t \end{bmatrix} \begin{Bmatrix} \Delta u_n \\ \Delta u_t \end{Bmatrix} \quad \text{Equation 16}$$

An initial set of dummy normal K_n and shear K_t stiffness is introduced by equation 16. Equation 17 stablishes the relation between the traction vector and the tangential stiffness matrix, D, and the relative displacements $\Delta\dot{u}$.

$$\dot{t} = D\,\Delta\dot{u} \quad \text{Equation 17}$$

$$D = \begin{bmatrix} D_{11} & D_{12} \\ D_{21} & D_{22} \end{bmatrix} \quad \text{Equation 18}$$

4.1.5 Parameters of the model

The different parameters required for the CSC model are explained in this section in detail:

- **Normal stiffness** (k_n). Corresponds to the stiffness of the mortar joint in the normal direction. The equation to obtain its value is the following (Lourenço, 1996):

$$k_n = \frac{E_u \times E_m}{h_m \times (E_u - E_m)} \quad \text{Equation 19}$$

where E_u is the Young modulus of the brick unit, E_m is the Young modulus of the mortar and h_m is the thickness of the mortar joint.

- **Shear stiffness** (k_t). Corresponds to the stiffness of the mortar joint in the tangent direction. The equation to obtain its value is the following:

$$k_t = \frac{G_u \times G_m}{h_m \times (G_u - G_m)} \qquad \text{Equation 20}$$

where G_u is the shear modulus of the brick unit, G_m is the shear modulus of the mortar and h_m is the thickness of the mortar joint.

- **Cohesion** (c). Corresponds to the maximum pure shear stress. The only requirement for its value is that it must be greater than zero: $c > 0$.

- **Friction angle** (ϕ). Corresponds to the slope of the Mohr-Coulomb friction mode. The only requirement for its value is: $0 \leq \phi < \frac{\pi}{2}$.

- **Dilatancy angle** (ψ). Corresponds to the angle defining the volume change in granular materials when subjected to shear deformations. The only requirement for its value is: $0 \leq \psi < \frac{\pi}{2}$.

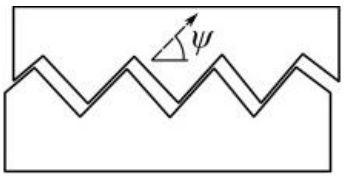

Figure 29. ***Dilatancy scheme (Kulyakhtin & V.Høyland, 2015).***

- **Residual friction angle** (ϕ_r). Corresponds to the friction angle after the failure of material. The only requirement for its value is: $0 \leq \psi < \frac{\pi}{2}$.

- **Confining normal stress** (σ_u). Confining normal stress for which the dilatancy coefficient is equal to zero. The only requirement for its value is: $\sigma_u < 0$.

- **Exponential degradation coefficient** (δ). Factor that determines how the dilatancy is depredated under shear-slipping deformations. The only requirement for its value is: $\delta < 0$.

$$\psi = \begin{cases} 0 \\ \psi_0 \left(1 - \frac{\sigma}{\sigma_u}\right)\left(1 - e^{-\delta v_p}\right) \\ \psi_0 e^{-\delta v_p} \end{cases}$$ Equation 21

- **Tensile strength** (f_t). Maximum tensile strength of the mortar joint. The only requirement for its value is: $0 \leq f_t \leq c/\tan(\phi)$.

- **Mode-I fracture energy** (G_f^I). Area defined by the tensile *stress – displacement* diagram. The only requirement for its value is: $G_f^I > 0$.

- **Mode-II fracture energy** (G_f^{II}). Area defined by the shear *stress – displacement* diagram. The only requirement for its value is: $G_f^{II} > 0$.

- **Compressive strength** (f_c). Maximum tensile strength of the mortar joint. The only requirement for its value is: $f_c > 0$.

- **Factor C_s**. This parameter controls the shear traction contribution to compressive failure. Its values must be $C_s > 0$.

- **Compressive fracture energy** (G_c). Area defined by the compression *stress – displacement* diagram. The only requirement for its value is: $G_c > 0$.

- **Equivalent plastic displacement** (k_p). Corresponds to the peak compressive stress (see Figure 27). The only requirement for its value is: $k_p > 0$.

4.1.6 Elemental test

Prior to the calibration of the model, a **dummy elemental test** has been carried out both with the experimental data from the experiments of Marastoni et al. (2016) and Pelà et al. (2017).

The purpose of this exercise is triple:

- First, **acquire skills with DIANA** in order to create the more complicated final model: learn how to create interfaces, apply increments of displacements on the boundary conditions, perform non-linear analyses, etc.

- Second, **understand the behavior of the masonry under different load combinations**: pure compression, pure traction, pure shear and a combination of all of them.

- Finally, the purpose is to check that the input data, i. e. the parameters obtained by Marastoni et al. (2016) and Pelà, et al. (2017) with the *Continuum* and *Interface Model* are correct.

The simple geometry of the elemental model is presented in the Figure 30. Two bricks of dimensions $100 \times 100\ mm^2$ with an **interface of mortar defined with the CSC interface model**.

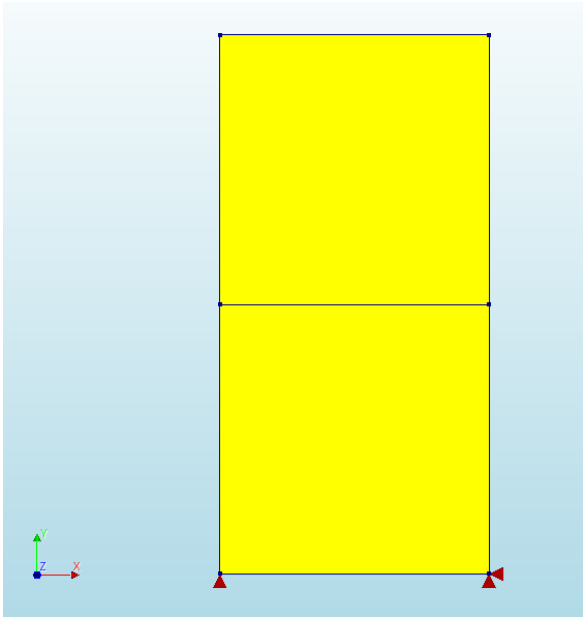

Figure 30. ***Geometry of the elemental test in DIANA.***

The parameters used for the brick (elastic) properties where the followings:

Parameter	Value	Units
Young modulus	9792	MPa
Poisson ratio	0,17	-
Density	2.400	kg/m3

Table 5. Parameters for the brick.

Once the geometry and the materials were defined, different combinations of loads are applied to the interface:

- **Pure compression** to check the compression strength f_c.
- **Pure tension** to check the tensile strength f_t.
- **Pure shear** to check the cohesion c.
- A c**ombination** of all the above to obtain the $\sigma - \tau$ diagram.

- **<u>Experimental data from Marastoni et al (2016)</u>**

The parameters of the CSC obtained from Marastoni et al. (2016) to be checked in this elemental test were the followings:

Parameter	Value	Units
Shear stiffness	10,66	MPa/mm
Normal stiffness	27,80	MPa/mm
Compressive strength	2,32	MPa
Tensile strength	0,35	MPa
Cohesion	0,32	MPa
Friction angle	32,32	o

Table 6. Parameters for the interface.

The results obtained with these values were the following ones:

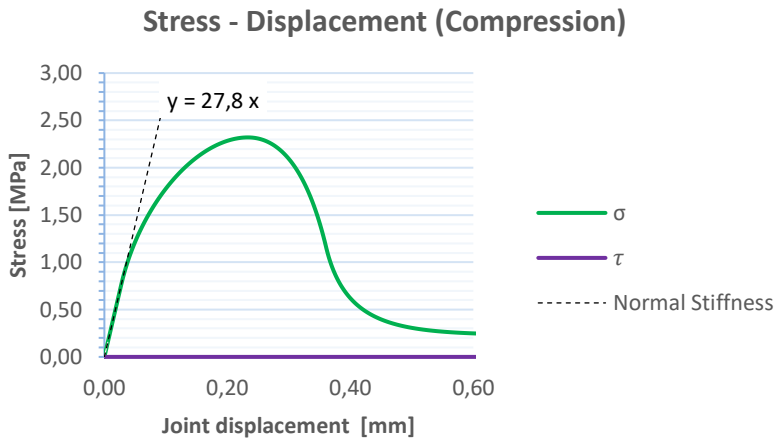

Figure 31. ***Results for the compression elemental test. Note that the normal stiffness and the compressive strength are correct (2,32 MPa and 27,80 MPa/mm).***

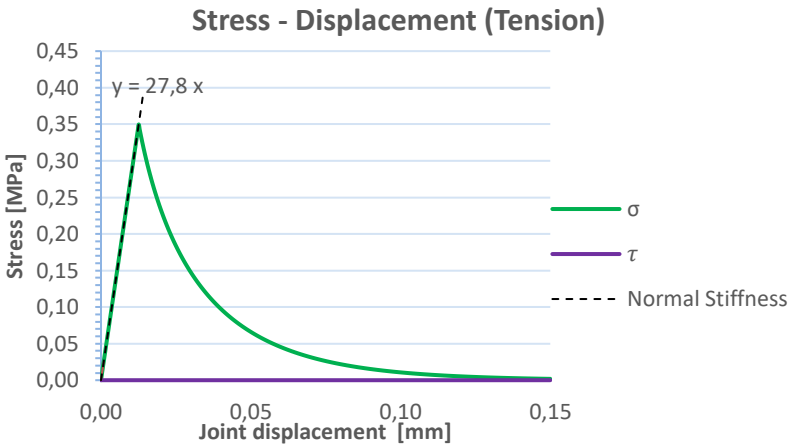

Figure 32. ***Results for the tension elemental test. Note that the normal stiffness and the tensile strength are correct (0,35 MPa and 27,80 MPa/mm).***

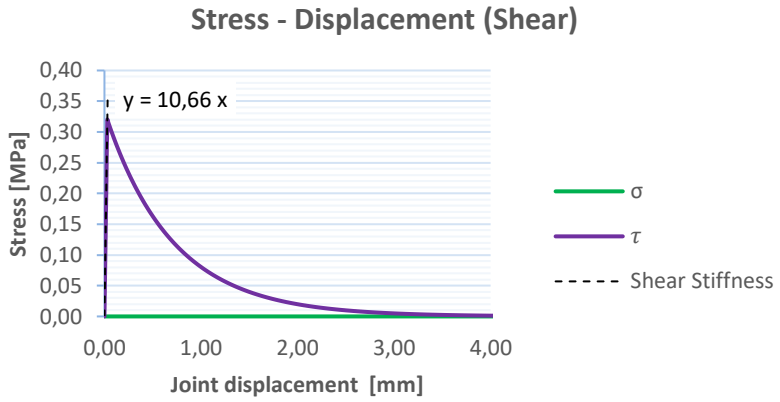

Figure 33. ***Results for the shear elemental test. Note that the shear stiffness and the cohesion are correct (0,32 MPa and 10,66 MPa/mm).***

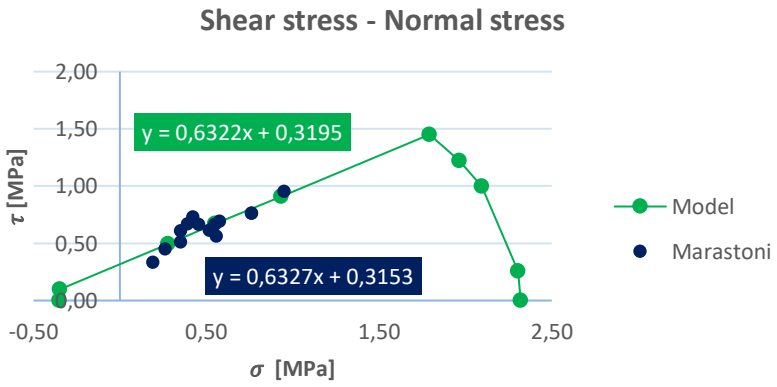

Figure 34. ***Results for the $\sigma - \tau$ diagram. Note that the cohesion (0,32 MPa) and the friction angle are very accurate (tan(32,32º)=0,6327).***

- **<u>Experimental data from Pelà et al. (2017)</u>**

The parameters of the CSC obtained from Pelà et al. (2017) to be checked in this elemental test were the followings:

Parameter	**Value**	**Units**
Compressive strength	1,02	MPa
Tensile strength	0,39	MPa
Cohesion	0,09	MPa
Friction angle	35,86	o

Table 7. Parameters for the brick.

Since neither the Young modulus, nor the shear modulus were measured in the study by Pelà et al., the values obtained by Marastoni et al. (2016) were used.

The results obtained with these values were the following ones:

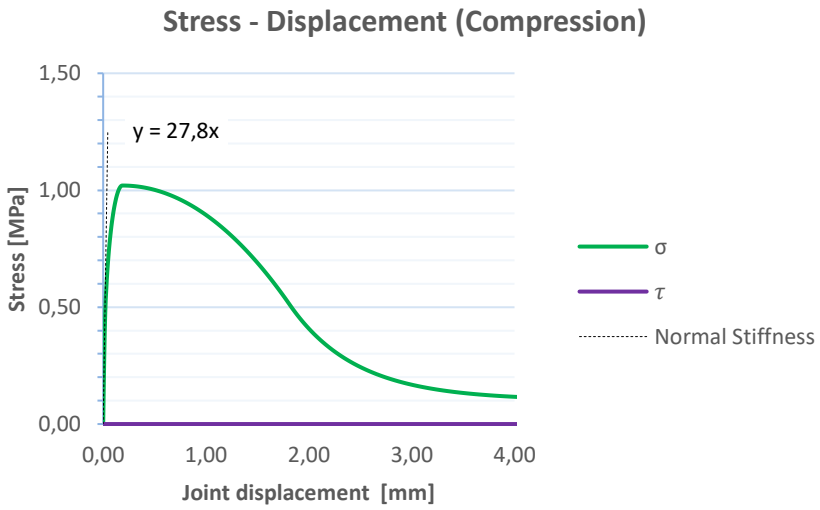

Figure 35. ***Results for the compression elemental test. Note that the normal stiffness and the compressive strength are correct (1,02 MPa).***

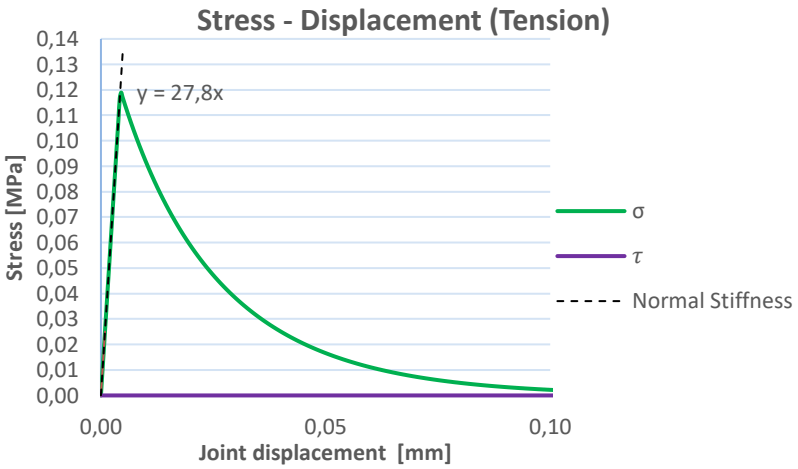

Figure 36. ***Results for the tension elemental test.***

Note that in the case of the tensile strength, the input value for the tensile strength f_t was 0,39 MPa but **the f_t obtained with the elemental model is 0,12 MPa**. The $\sigma - \tau$ diagram explains this behavior:

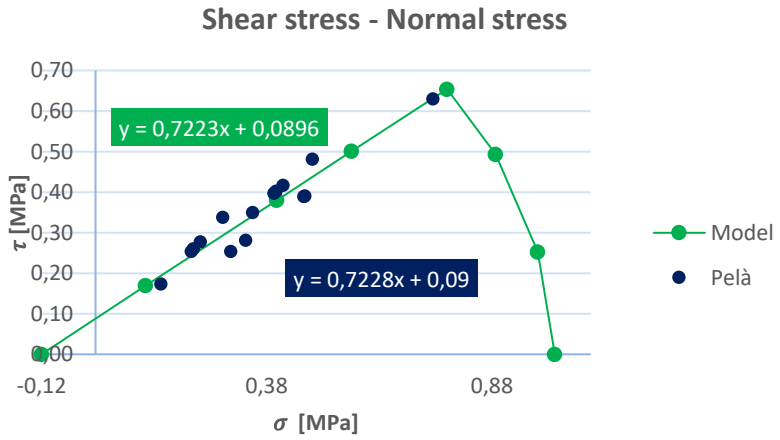

Figure 37. ***Results for the $\sigma - \tau$ diagram. Note that the cohesion (0,09 MPa) and the friction angle are very accurate (tan(35,86º)=0,7228).***

The $\sigma - \tau$ diagram shows that **for a cohesion of 0,09 MPa and a friction angle of 35,86º, the tensile strength will never go further than 0,12 MPa**.

This is a remarkable success of this element model: thanks to this elemental exercise, **the tensile strength has been adjusted** prior to the calibration process.

Finally, the shear stress performs also a good behavior:

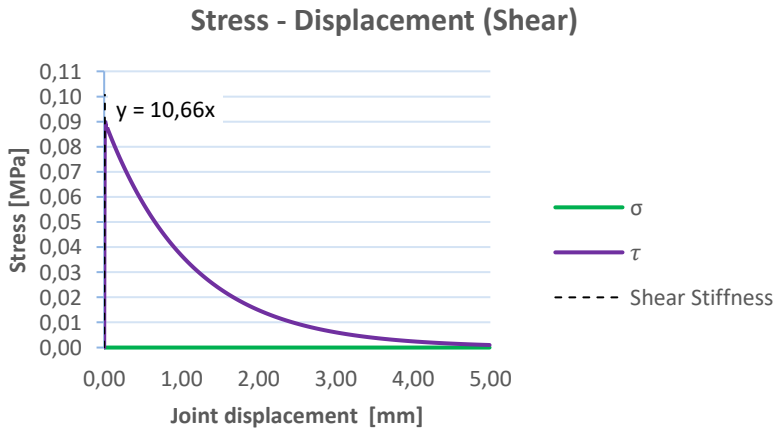

Figure 38. ***Results for the shear elemental test. Note that the shear stiffness and the cohesion are correct (0,09 MPa).***

The elemental test exercise has proved to be useful to check the behavior of the CSC model and to **calibrate correctly the parameters** derived from the experimental campaign into the numerical micromodel.

4.2 FEM model

In this thesis, with the objective of modeling a specimen subjected to a shear test, a **simplified 2-D plain strain micromodel** has been chosen.

On the one hand, the use of a **2-D model** (plain strain) allows to reduce drastically the computational cost, especially considering that the depth of the samples (dimension avoided) is close to 150 mm, while the diameter of the samples (dimension analyzed) is close to 90 mm. Therefore, this simplification allows to avoid a huge number of finite elements and, thus, reduce the computational cost.

On the other hand, a **simplified model** has proved to be accurate enough to represent the shear behavior of the brick-interface model. The results obtained and their accuracy are presented in further sections of this thesis.

4.3 Calibration of the model: sensitivity analysis

In order to evaluate the influence of the main parameters defining the numerical model presented in the previous chapter, several sensitivity analyses have been carried out.

In all the sections inside this chapter, the analysis has the same structure: the *Load – Joint relative displacement* diagram is presented for each experimental campaign and angle (45º, 50º, 55º and 60º for Marastoni et al. (2016) and 40º, 45º and 50º for Pelà et al. (2017)).

In the graphs, the grey line color represents the experimental results, whilst the red, blue and green lines represent the numerical ones for different values of the parameter analyzed. Note that the **green line** always **corresponds to the final value** of the parameter chosen for the model after the calibration process, so the reader of this document can get an idea of the influence of the parameter chosen.

An important issue is that, during the calibration process, the parameters of the CSC relatives to the **tensile strength remained constant** for any value assigned to them. The reason for that is that **in the Brazilian Test, no pure tensile stress is obtained in the brick-mortar interface**, only compression and/or shear, depending on the angle. Therefore, the tensile parameters calibration has been excluded in this section since no information could be extracted from its calibration.

Finally, following this last reasoning:

- The **compressive parameters** were calibrated using the results of **lower angles** of the experimental campaigns (45^o for Marastoni et al. (2016) and 40^o for Pelà et al. (2017)).
- On the other hand, the **shear parameters** were calibrated with the **higher angles** (60^o for Marastoni et al. (2016) and 50^o for Pelà et al. (2017)).

As a final comment, some values used in the calibration were obtained from the **literature** whilst others were just obtained by **trial and error**. All the criteria followed to determine them is presented in the analysis.

4.3.1 Data calibration for the campaign of Marastoni et al. (2016)

In this section, the parameters of the CSC model are calibrated using the data of the experimental campaign carried out by Marastoni et al. (2016). The result for each value tested is presented as well as a justification for its behavior.

4.3.1.1 Dilatancy sensibility

The **dilatancy** (ψ) values tested in the calibration were:

- $\psi = 0{,}5641$ rad. This is the maximum value tested and corresponds to the value of the friction angle ($\phi = 32{,}32^o = 0{,}5641\ rad$). This approach is known as the ***associated flow rule*** (Brocato & Mondardini, 2011) and consists on assume a **dilatancy angle equal to the friction angle**.
- $\psi = 0{,}5500$ rad. This value has been calibrated to acquire the best results in terms of agreement with the experimental campaign.
- $\psi = 0{,}0000$ rad. This minimum value is proposed by many authors as a simplification, meaning that the dilatancy contribution to the resistance of the mortar is null (Miccoli, et al., 2014).

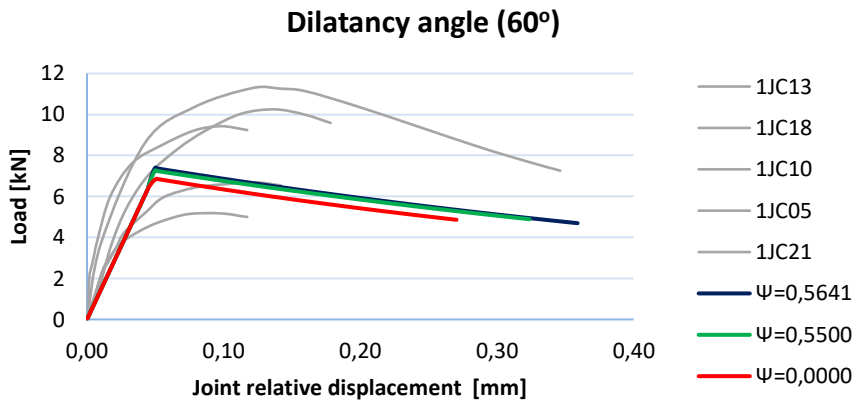

Figure 39. *Dilatancy analysis.*

According to the results, the difference between $\psi = 0{,}5641$ and $\psi = 0{,}5500$ rad is less than 2%. On the other hand, a null dilatancy represents a reduction of 8% for the maximum strength.

This behavior is expected: **for lower values of dilatancy**, **the confinement of the mortar joint decreases** and, therefore, **the final strength of the specimen drops**.

4.3.1.2 Residual friction angle sensibility

The **residual friction angle** (ϕ_{res}) values tested in the calibration were:

- $\phi_{res} = 0{,}5641$ rad. This is the maximum value tested and, again, corresponds to the value of the friction angle ($\phi = 32{,}32^o = 0{,}5641\ rad$). The physical meaning of this approach is that there is **no reduction of the friction angle for the residual strength**.

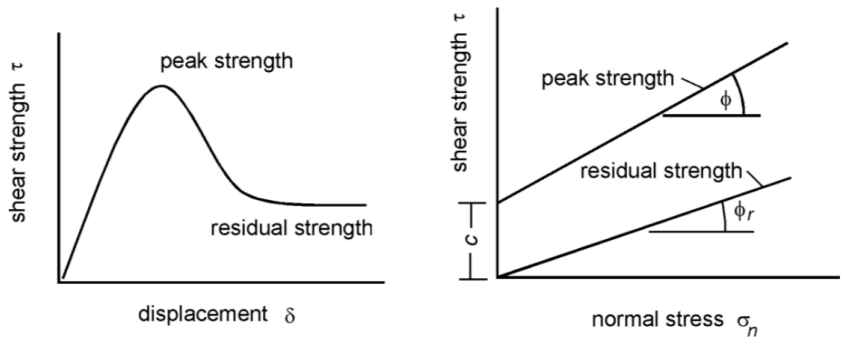

Figure 40. *Differences between the friction angle and the residual friction angle (Rocscience, 13).*

- $\phi_{res} = 0{,}5077$ rad. This value has been chosen as an approximation of $\phi_{res} \approx 0{,}90 \times \phi$ obtained by Siamak Sattar (Sattar, 2013).
- $\phi_{res} = 0{,}0000$ rad. This minimum value has been as an extreme value to see a big range of results (going from $0{,}5641$ to $0{,}0000$).

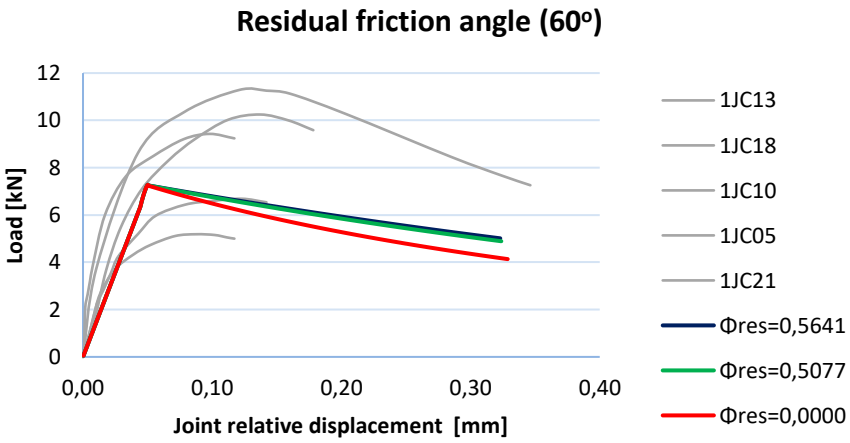

Figure 41. *Residual friction angle analysis.*

The maximum strength obtained for all three values tested are the same. The big difference comes with decreasing of the strength after the peak: as expected, **for lower values of ϕ_{res}, the strength decreases faster** (see Figure 40).

4.3.1.3 Confining normal stress sensibility

The **confining normal** (σ_u) values tested in the calibration were:

- $\sigma_u = -1$ MPa. This value has been chosen as a starting point to calibrate the confining normal stress since it is widely used in literature (Lourenço, 1996 and Li, et al., 2013).

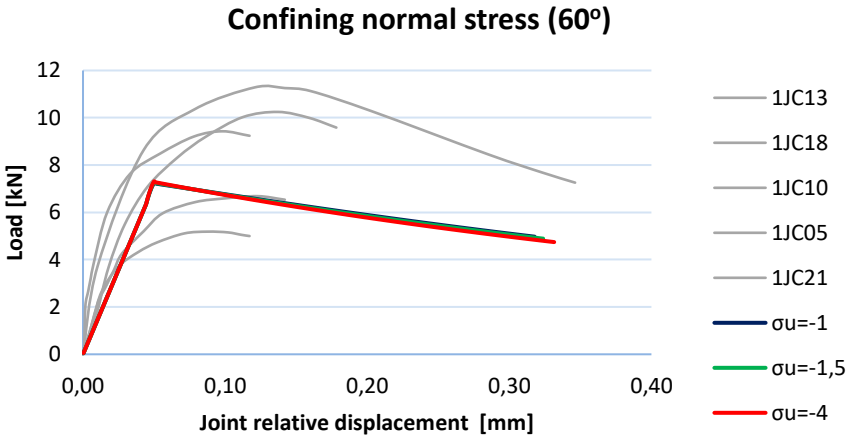

Figure 42. *Confining normal stress analysis.*

- $\sigma_u = -1{,}5$ MPa. This value has been calibrated to acquire the best results in terms of agreement with the experimental campaign.
- $\sigma_u = -4$ MPa. This extreme value has been chosen to obtain a wide range of results to observe the behavior of the model.

According to the results, the difference between the tested values is below 1%. However, the biggest confining normal stresses, $\sigma_u = -4$ MPa, exhibits a little higher maximum strength. This was expected, since the confining normal stress corresponds to the normal stress for which the dilatancy coefficient is equal to zero. Therefore, the higher the magnitude of σ_u, the latter dilatancy goes to zero, and the higher maximum strength obtained.

4.3.1.4 Exponential degradation parameter sensibility

No literature establishing a relation for this parameter was found. Therefore, arbitrary values were chosen:

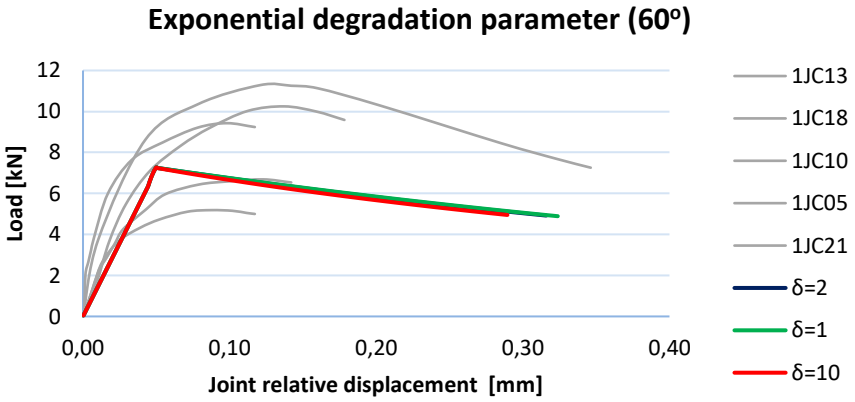

Figure 43. *Exponential degradation coefficient analysis.*

As expected, **for higher values of the degradation coefficient, the strength decreases faster** after the peak.

4.3.1.5 Mode-II fracture energy sensibility

The **Mode-II fracture energy** (G_f^{II}) values tested in the calibration were:

- $G_f^{II} = 0{,}1\ \mathrm{N/mm}$. This value has been chosen as an extreme value.
- $G_f^{II} = 0{,}23\ \mathrm{N/mm}$. This value has been calibrated to acquire the best results in terms of agreement with the experimental campaign. The calibrated value of another author was used as a reference (Oliveira & Correa, 2017).
- $G_f^{II} = 1\ \mathrm{N/mm}$. Again, this is an extreme value selected arbitrary.

According to the theory presented before, for higher values of G_f^{II}, the area under the curve (energy necessary to break the material) increases:

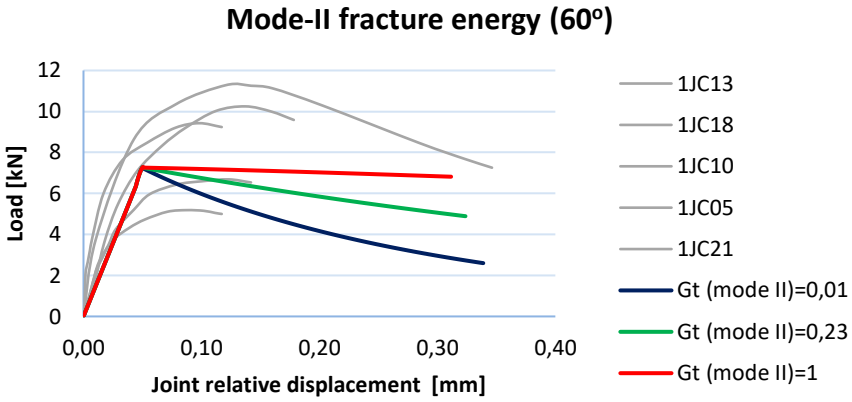

Figure 44. *Mode-II fracture energy analysis.*

4.3.1.6 Compressive fracture energy sensibility

Note that from this moment on, since the parameters to be calibrated will be related to the **compressive behavior**, the experimental samples used to calibrate these parameters will be the ones obtained with lower angles of the mortar joint, i. e. with higher compression in the interface (45º).

However, in the case of the experimental data of Marastoni et al. (2016), 45º seems not to be enough to calibrate the compressive fracture energy since all the values tested exhibit the same result. The reason for this is that **the shear phenomena dominates over the compressive** and, therefore, the post-peak shape of the curve is determined only by the Mode-II fracture energy.

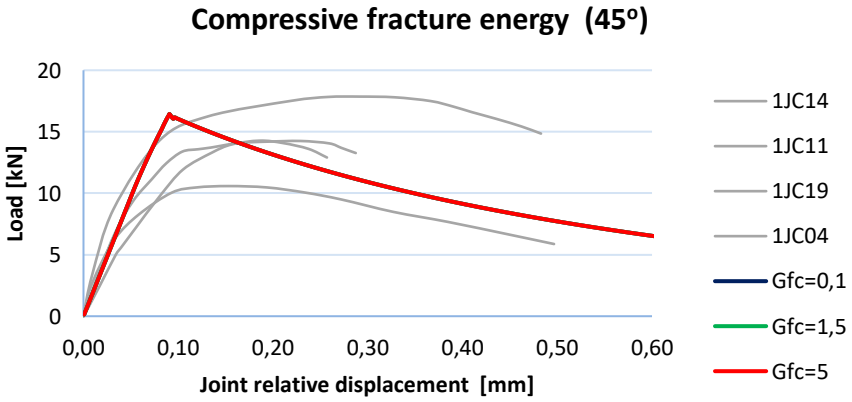

Figure 45.*Compressive fracture energy analysis.*

4.3.1.7 Equivalent plastic relative displacement sensibility

The **equivalent plastic relative displacement** (k_p) values tested in the calibration were chosen arbitrary:

- $k_p = 0{,}01$.
- $k_p = 0{,}15$. This value has been calibrated to acquire the best results in terms of agreement with the experimental campaign.
- $k_p = 1$.

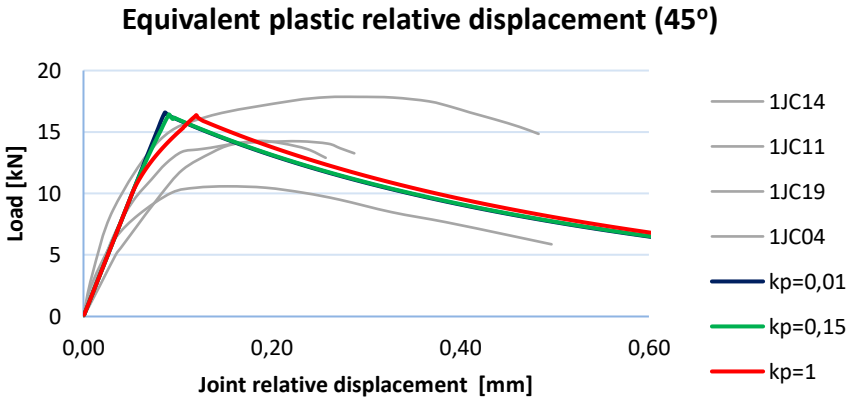

Figure 46. *Equivalent plastic relative displacement analysis.*

The results are consistent with the theory showed earlier in figure 27 when the compression cap of the CSC model was presented: k_p is related with the peak of the *Load – Displacement* graph (the higher the k_p, the more relative displacement of the joint takes to arrive to the peak of the curve).

4.3.1.8 Factor C_s sensibility

The values tested in the calibration for this parameter controlling the shear traction contribution to compressive failure were arbitrary chosen:

- $C_s = 1$.
- $C_s = 3$.
- $C_s = 5$.

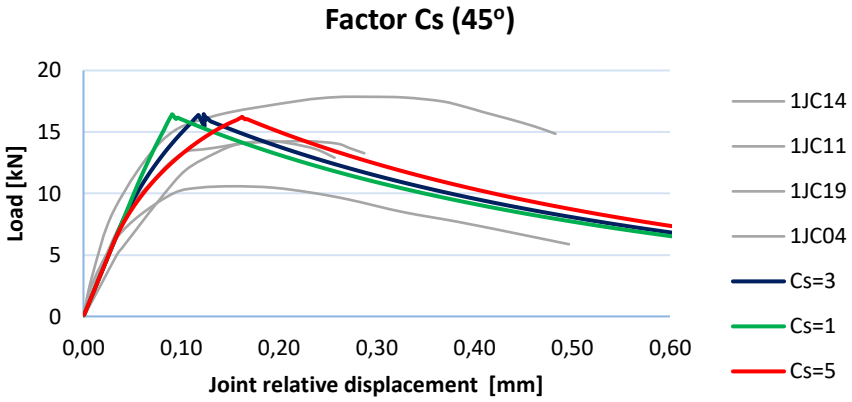

Figure 47. ***Factor Cs analysis.***

The case of Factor C_s is analyzed in detail in the Results section, since it provided very interesting results during its calibration. Apart from the results shown in Figure 47, other results were obtained to calibrate its value. All the process is discussed in the Results section.

4.3.2 Data calibration for the campaign of Pelà et al. (2017)

In this section, the parameters of the CSC model are calibrated using the data obtained in the experimental campaign carried out by Pelà et al. (2017).

All **the procedure to obtain the values is the same followed in the previous section**. Therefore, to avoid redundancy in the explanation, only the graphs are presented now, with no justification for the values chosen (the justification is the same defined for the data of Marastoni et al. (2016)).

The only remarkable difference with the results obtained in the previous section occurs for the compressive fracture energy. As explained before, with the samples of Marastoni et al. (2016) it was not possible to calibrate G_c (the lower angle of the samples was 45º). However, with the samples used by Pelà et al. (2017), it is possible to calibrate it, since the lower angle is 40º and the compressive energy dominates over the Mode-I fracture energy:

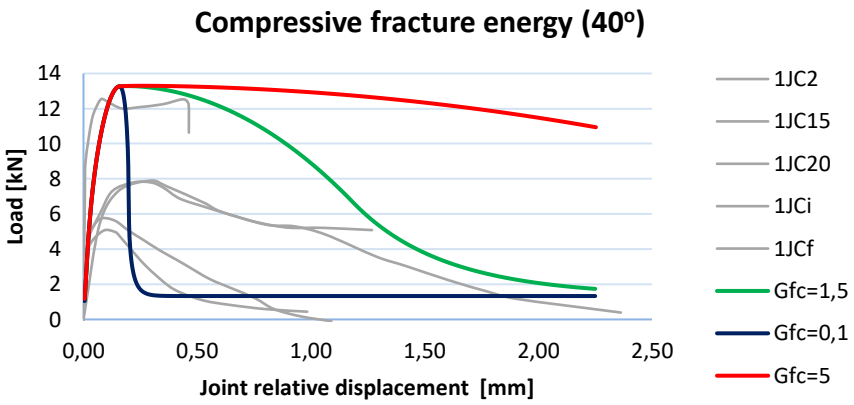

Figure 48.*Compressive fracture energy analysis.*

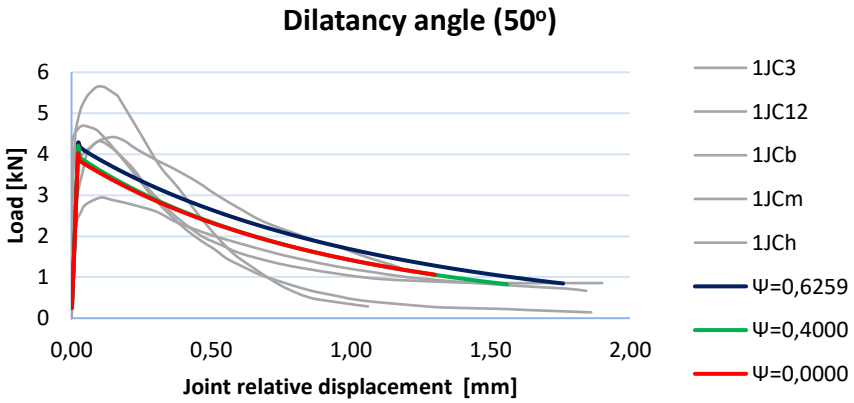

Figure 49. *Dilatancy analysis.*

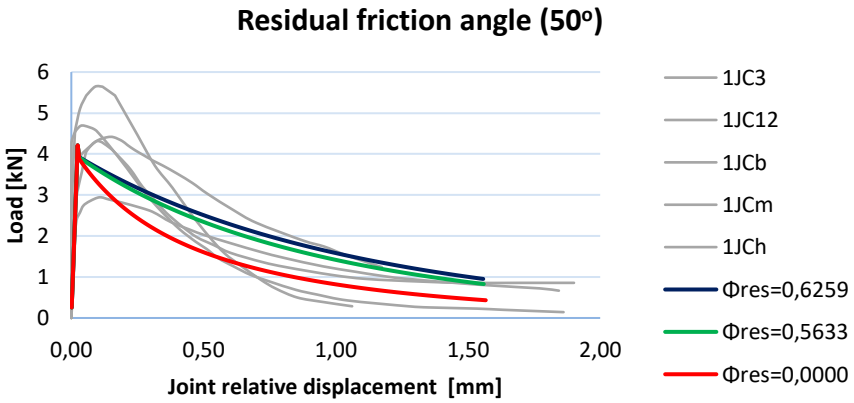

Figure 50. *Residual friction angle analysis.*

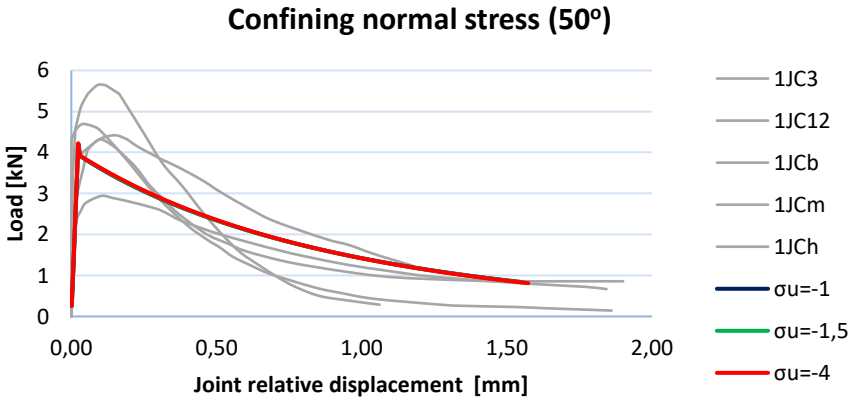

Figure 51. *Confining normal stress analysis.*

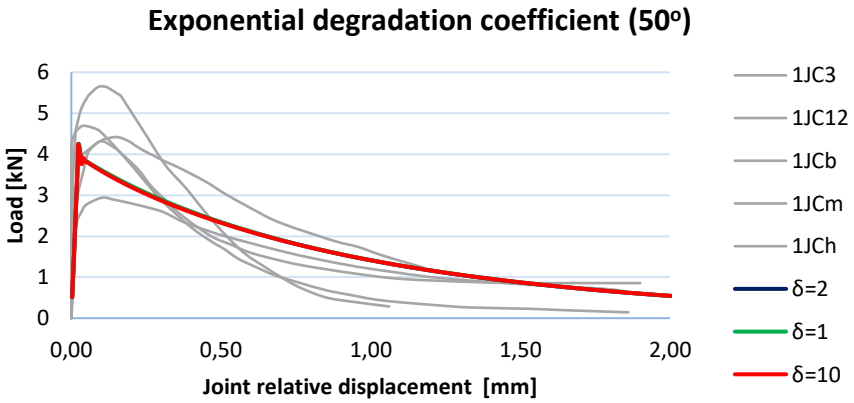

Figure 52. *Exponential degradation coefficient analysis.*

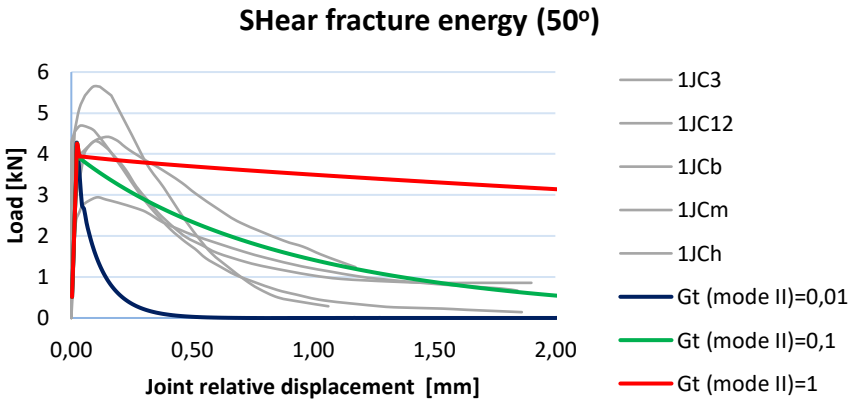

Figure 53.*Mode-II fracture energy analysis.*

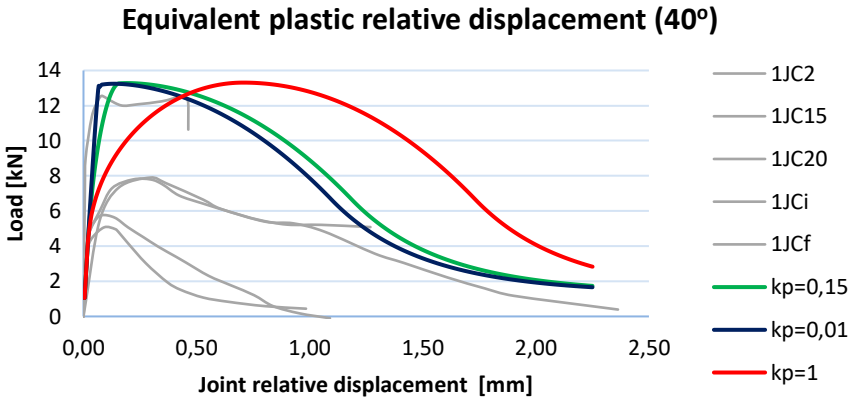

Figure 54. *Equivalent plastic relative displacement analysis.*

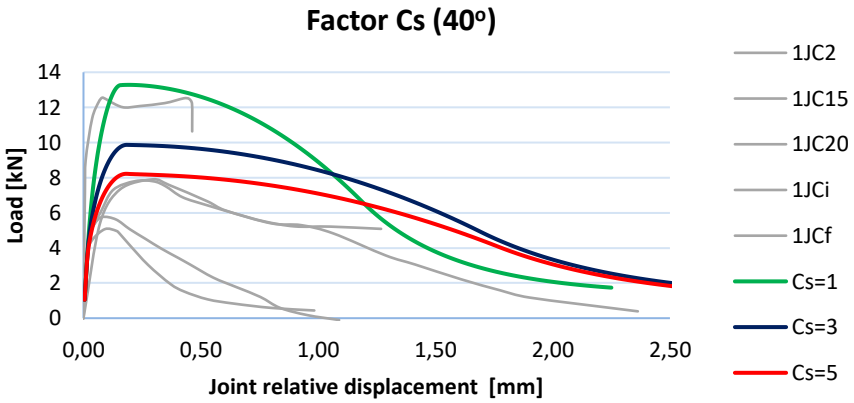

Figure 55. *Factor Cs analysis.*

4.3.3 Automatization of the calibration process

The **calibration process** of models is a very **time-consuming task** since a great number of parameters have to be tested. Besides, **only one parameter can be tested at a time**.

One of the tasks carried out during this thesis was the development of a procedure that could **automatize** in some way this process. To do so, two approaches have been followed:

- **Generation of automatic reports**. DIANA 10.2 provides a feature that allows to predefine reports for the model. By doing this, right after every simulation, all that is needed to obtain the output (graphs, tables, text, etc..)

is to click the "*generate report"* button in the report section and all the desired data is saved in a file (.word, .html, Markdown, etc.).

It must be noted that the alternative, i. e. doing this report manually, means to follow a long process through the DIANA interface: access the results window, select the element of the mesh for which the results are needed, open a table with variable of interest (displacement, stress, strain, etc.), copy the table to the program desired to obtain the graphs (typically Excel), etc. By using the automatic reports, this long process is skipped. An example of the output generated for the elemental test described in section "4.1.6. Elemental test" is presented in "Appendix 1" at the end of this Memory.

- **DIANA scripts**. There is also the possibility to give the inputs to DIANA through scripts, instead of manually, since DIANA supports Python. Happily, no programming skills are needed to use this feature. All the necessary is to do one calibration manually (just the first time). Once this is done, select "Save script" in the File options. This action will save all the tasks done in a python script. What must be done then, is to open the script as a .txt file to access this information. Then, the approach consists on copy/paste the code in the same script but changing the value of the parameters to be calibrated in each copy/paste. Then, the new script can be run from DIANA using the option "Run saved script" and all the simulations and reports for the different parameters will be generated automatically.

4.4 Final model

4.4.1 Geometry and boundary conditions

The final geometry of has been defined in a way that can be applied to simulate all the range of angles used in the experimental campaign, i.e. from 40º to 60º, using the ***rotation*** feature provided by DIANA FEA.

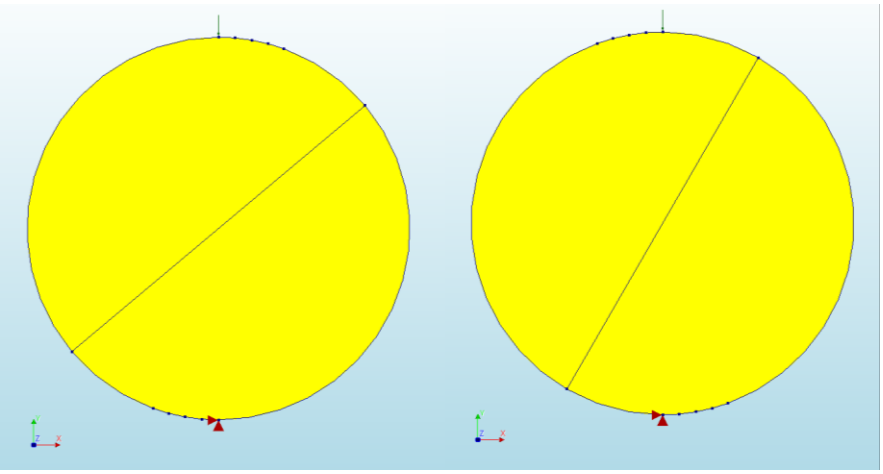

Figure 56. *Final geometry, boundary conditions and prescribed displacement of the micro-model (40º in the left, 60º in the right).*

The geometry of the cylindrical specimen is **defined by two halves of brick joined by a line interface element**. The boundary conditions of the bottom of the sample are defined as an **embedment** (restricted displacement in the X and Y axis and rotation over the Z axis). On the top vertex of the specimen, a **vertical prescribed displacement** is applied to be able to perform a *displacement-controlled* analysis.

The geometry is defined as **plane strain** and the dimension of the circumference corresponds to **90 mm**, according to experimental data.

4.4.2 Parameters

4.4.2.1 Brick

To obtain the final model, the brick is defined as a **continuum element with linear elastic properties**. Its mechanical properties were obtained from the study of Marastoni et al. (2016) and the density was supposed as 2.400 kg/m^3 since it was not measured in the study.

Symbol	*Parameter*	*Value*	*Units*
E_u	Young Modulus brick	9792,00	MPa
v_u	Poisson unit	0,17	-
ρ_u	Density unit	2.400	kg/m^3

Table 8. Brick final model parameters.

The same parameters for the simulation of both campaigns are used, since no data from the unit bricks was presented in the work of Pelà, et al.

4.4.2.2 Mortar interface

- The **Mode-I fracture energy** was obtained from the literature, and it was not possible to carry out any calibration since no tensile stress is applied to the interface.

  The formula to calculate this parameter is (Lourenço and Oliveira, 2014):

$$G_f^I = 0{,}029 \times f_t \qquad \text{Equation 22}$$

- The **tensile strength f_t** in the case of Marastoni, was taken directly from the paper. For the case of Pelà, et al., was adjusted after the results obtained with the elemental test described in previous sections.

- The **normal stiffnesses k_n** was calculated using the equations provided in the literature (Lourenço, 1996):

$$k_n = \frac{E_u \times E_m}{h_m \times (E_u - E_m)} \qquad \text{Equation 23}$$

  where E_u is the Young modulus of the brick unit, E_m is the Young modulus of the mortar and h_m is the thickness of the mortar joint, all of the obtained from the study of Marastoni et al. (2016). Since these parameters were not available in the study of Pelà, et al., the same value for the normal stiffness was used in both simulations.

- To calculate the **shear stiffness k_t** the following parameters are needed: the shear modulus of the brick unit G_u, the shear modulus of the mortar G_m and the thickness of the mortar joint h_m. In the case of Marastoni et al. (2016), G_m was estimated and h_m was measured, but there is no estimation for the value of G_u. The approach followed in this thesis consists on assume that the material is isotropic and, therefore, the G_u can be calculated from the unit Young modulus:

$$G_u = \frac{E_u}{2 \times (1 + \nu_u)}$$ Equation 24

Now, the shear stiffness can be calculated as:

$$k_t = \frac{G_u \times G_m}{h_m \times (G_u - G_m)}$$ Equation 25

Again, since these parameters were not available in the study of Pelà, et al., the same value for the shear stiffness was used in both simulations.

The rest of the parameters were either obtained from the experimental data provided by the two authors described in this thesis or obtained from the calibration process described in the chapter before. All the mortar interface parameters are summarized in the following table:

Symbol	*Parameter*	*Marastoni, et al. Model*	*Pelà, et al. Model*	*Units*
k_n	Normal Stiffness	27,80	27,80	MPa/mm
k_t	Shear Stiffness	10,66	10,66	MPa/mm
f_{tm}	Tensile strength	0,35	0,12	MPa
G_t *(mode I)*	Tensile fracture energy	0,010	0,011	N/mm
C	Cohesion	0,32	0,09	MPa
Φ	Friction angle	0,5641	0,6259	rad
ψ	Dilatancy angle	0,5500	0,0000	rad
Φ_{res}	Residual friction angle	0,5077	0,5633	rad
σ_u	Confining normal stress	-1,5	-1,5	Mpa
δ	Exponential degradation parameter	1	1	-
G_t *(mode II)*	Shear fracture energy	0,23	0,10	N/mm
f_{cm}	Compressive strength	2,32	1,02	MPa
C_s	Factor Cs	1	1	-
G_{fc}	Compressive fracture energy	1,5	1,5	N/mm
k_p	Equivalent plastic relative displacement	0,15	0,15	-

Table 9. Mortar interface mechanical properties for each model.

4.4.2.3 Mesh

The mesh of the final micro-model (see Figure 57) has been chosen according to a convergence analysis described in this section.

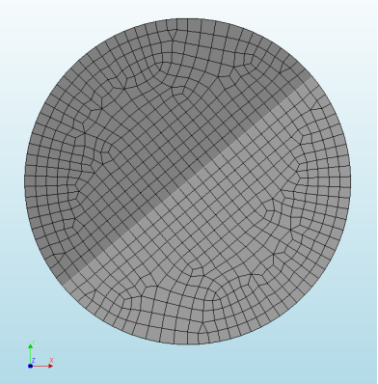

Figure 57. ***Final micro-model mesh.***

The elements available to mesh the geometry (plane strain) are quadrilateral, triangular and interface elements:

- The **interface elements** correspond to the L8IF elements provided in DIANA 10.2. These elements are based on linear interpolation and a 2-point Newton-Cotes integration scheme:

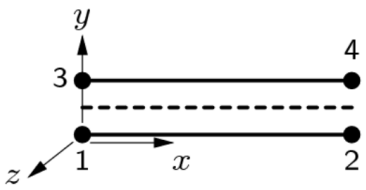

Figure 58. ***Interface element: L8IF (DIANA, 2017).***

- The **brick** is simulated with Q8EPS and T6EPS elements provided in DIANA 10.2. The Q8EPS element is a four-node quadrilateral isoparametric plane strain element based on linear interpolation and Gauss integration. The T6EPS element is a three-node triangular isoparametric plane strain element, also based on linear interpolation and Gauss integration.

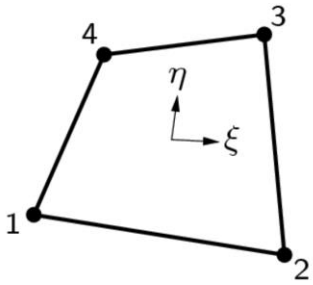

Figure 59. ***Interface element: Q8EPS (DIANA, 2017).***

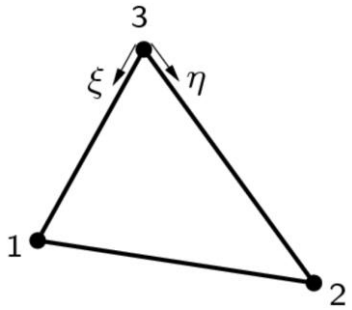

Figure 60. ***Interface element: T6EPS (DIANA, 2017).***

A **mesh convergence analysis** was performed in order to determine the optimal mesh size in terms of accuracy and computational cost. The measurement used to compare the results correspond to the maximum normal stress obtained in the middle point of the interface with a slope of 45º. Two approaches were used:

- **Triangular elements** for the brick and **interface elements** for the joint:

α [°]	*Element size [mm]*	*Brick type of element*	*Interface type of el.*	*N. of nodes*	σ_{max} *[MPa]*	E_{rel}
45	10	T6EPS	L8IF	118	0,8868	0,0041
45	5	T6EPS	L8IF	342	0,8926	0,0024
45	3	T6EPS	L8IF	866	0,8921	0,0018
45	2	T6EPS	L8IF	1992	0,8909	0,0005
45	1	T6EPS	L8IF	-	0,8905	-

Table 10. Triangular convergence elements

- **Quadrilateral elements** for the brick and **interface elements** for the joint:

α [°]	Element size [mm]	Brick type of element	Interface type of el.	N. of nodes	σ_{max} [MPa]	E_{rel}
45	10	Q8EPS	L8IF	102	0,8971	0,0059
45	5	Q8EPS	L8IF	330	0,8934	0,0017
45	3	Q8EPS	L8IF	816	0,8924	0,0006
45	2	Q8EPS	L8IF	1758	0,8920	0,0002
45	1	Q8EPS	L8IF	-	0,8919	-

Table 11. Quadrilateral convergence elements.

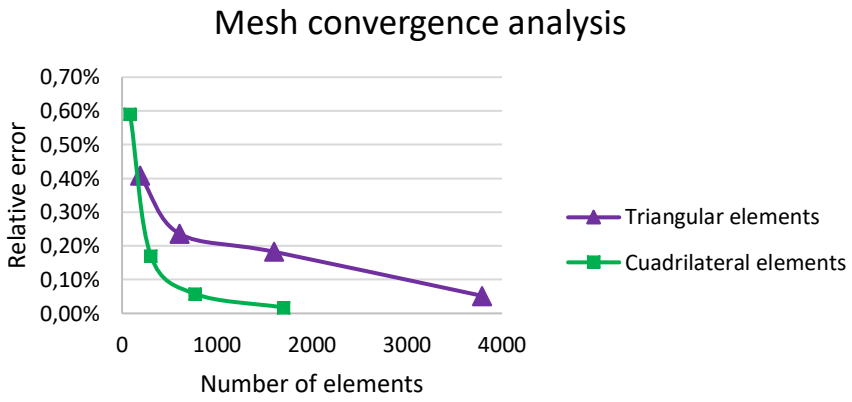

Figure 61. *Mesh convergence analysis.*

A final mesh of **quadrilateral elements with 3 mm** size is chosen, since it provides a solution (x) with a great accuracy: less than 0,10% of relative error, assuming the result obtained with the finest element (1 mm) as the reference solution (x′).

$$E_{rel} = \frac{x - x'}{x'} \qquad \text{Equation 26}$$

4.4.2.4 Iterative method

The iterative method used in the analysis corresponds to the **Regular Newton-Raphson Method** with 10 maximum iterations.

This method yields a **quadratic convergence**, which means that the method converges to the final solution within only a few iterations. A disadvantage of

the method is that the stiffness matrix has to be set up at each iteration and, if a direct solver is used to solve the linear set of equations, the time-consuming decomposition of the matrix has to be performed at every iteration as well (DIANA, 2017).

However, in the model created in this thesis, the Regular Newton-Raphson Method performed reasonably fast since the mesh is not too fine.

4.4.2.5 Displacement increments

Displacement-controlled tests allow to obtain the post-peak softening branch of the force – displacement diagram. Therefore, this method is used both in the experimental campaign and in the numerical model.

As a general value, the vertical prescribed displacement used in the model corresponds to 0,002 mm applied in 500 steps (equal to 1 mm). However, depending on the slope of the interface, the displacement increment is adjusted to obtain the desired *load – displacement* graph.

Chapter 5. Results

The correct interpretation of the results is aimed to improve the knowledge about the phenomena that occurs in the brick-mortar interface under shear stress.

In this chapter, the results obtained for the simulation of the two experimental campaigns described before, are presented and analyzed.

5.1 Load – Displacement curves

Figure 62 present the *Load – Displacement* curves obtained for the simulation of the campaign carried out by Marastoni et al. (2016):

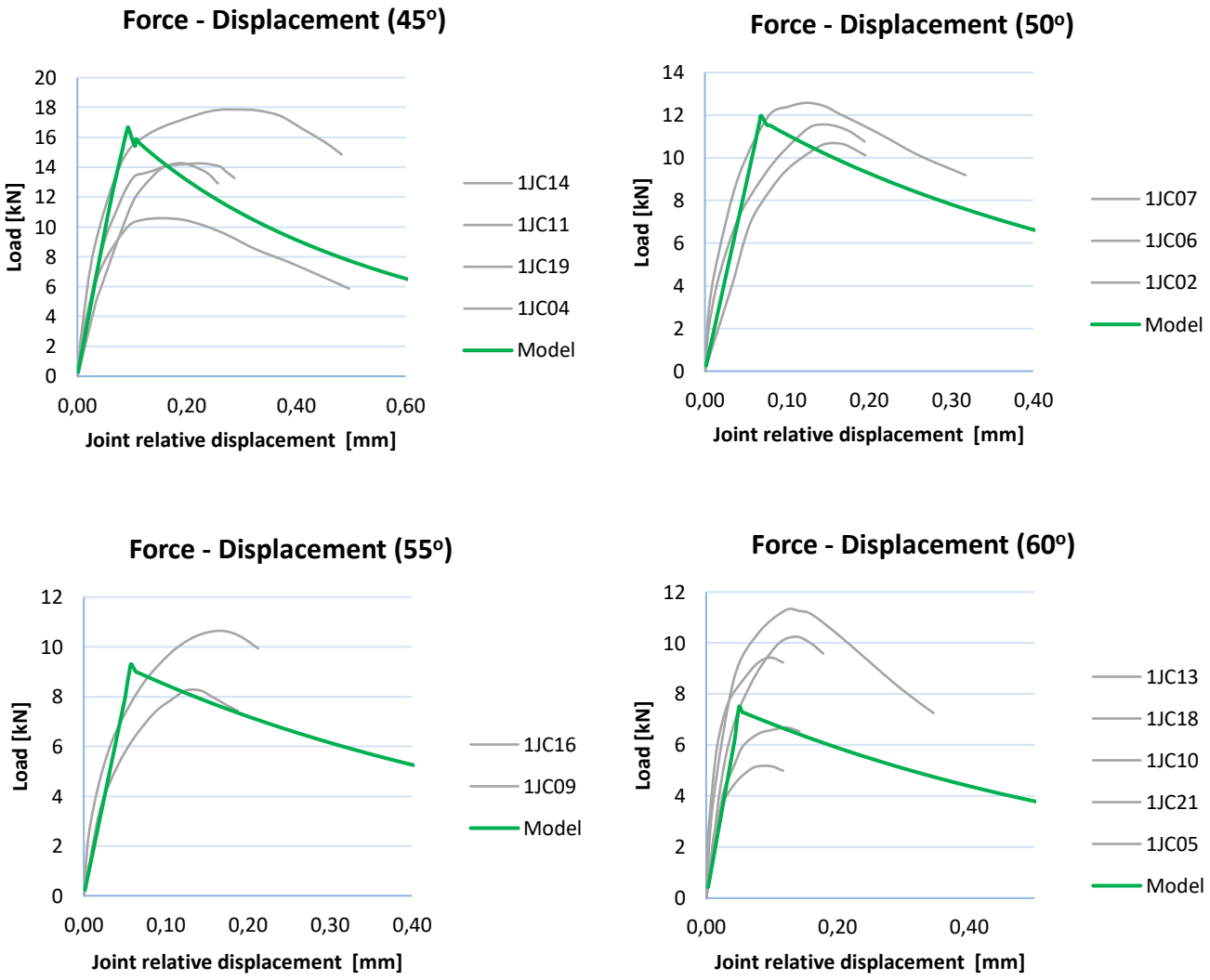

Figure 62. ***Load – Displacement curves for Marastoni, et al. simulation.***

The curves obtained with the model present a **good correlation** regarding the experimental data. It must be considered that **the experimental curves present a big dispersion**. For these reason, it is very difficult to create a model that fully represent the experimental curves.

Analyzing the curves in detail, for the lowest angles (40º and 50º) it is observed that the model predicts a maximum resistance higher than the average obtained in the tests. The opposite happens for bigger angles (specially for 60º), where the model predicts a maximum strength lower than the average obtained in the experimental campaign.

This behavior indicates that the model presented in this study, **slightly overestimate the compression stress and underestimate the shear** one. However, the results obtained are satisfactory given the scatter of the experimental data.

Figure 63 presents the *Load – Displacement* curves obtained for the simulation of the campaign of Pelà, et al. (2017):

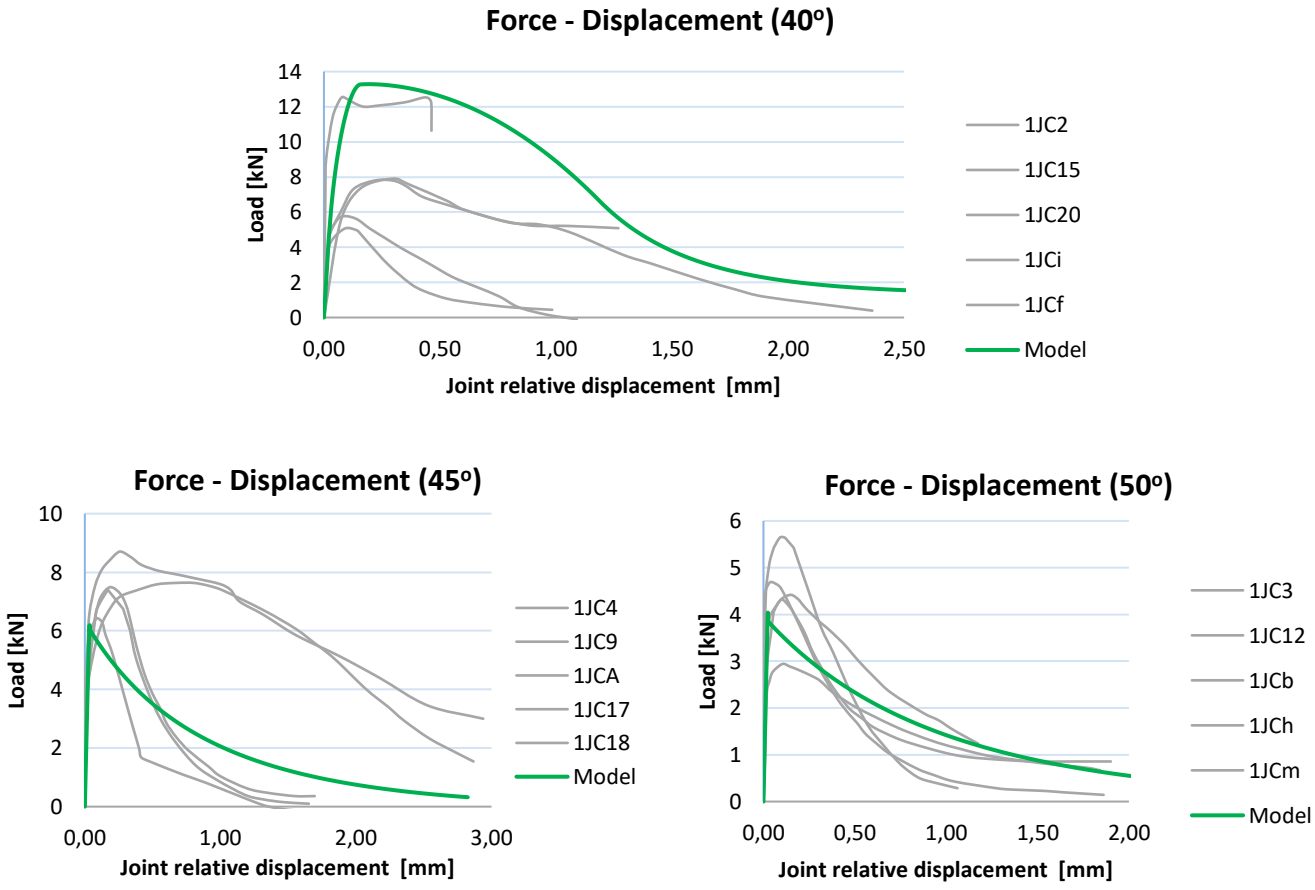

Figure 63. ***Load – Displacement curves for Pelà, et al. simulation.***

In the case of the simulation for the campaign of Pelà et al. (2017), the model presents the same behavior described for Marastoni et. al (2016), even more clearly in the case of 40^0. This confirms the hypothesis that the model overestimates the compression for small angles.

In the case of 40^0, it should be noted the huge dispersion obtained in the experimental campaign. However, even considering the wide range of experimental results, the numerical model seems to be overestimating the compressive stress.

5.2 Stress distribution along the specimen

In this section, the stresses in the global axis X (S_{xx}) and Y (S_{yy}) are presented. The purpose of this chapter is to understand how the stresses are distributed through the bricks until they arrive to the interface. **All the stresses presented in this section correspond to the step in which the peak strength of that sample is reached**.

Since the prescribed displacement, that simulates the load in the Brazilian test, is applied in the top node of the geometry, the stresses in the elements surrounding this area suffer a concentration of stresses. This is normal in FEM models. The problem is that since there are elements with stresses much higher than others, it is not possible to obtain plots in which the distribution of stresses with different colors is appreciated. To avoid this, **the minimum/maximum value of the legend has been limited** to obtain a distribution of stresses that is visible. Therefore, the figures presented in this section, provide an idea of the distribution of stresses, not real maximum/minimum values.

5.2.1 Marastoni et al. (2016)

The following figures present the stresses S_{xx} and S_{yy} for the specimens tested at 45^o, 50^o, 55^o and 60^o simulating the test carried out by Marastoni et al. (2016).

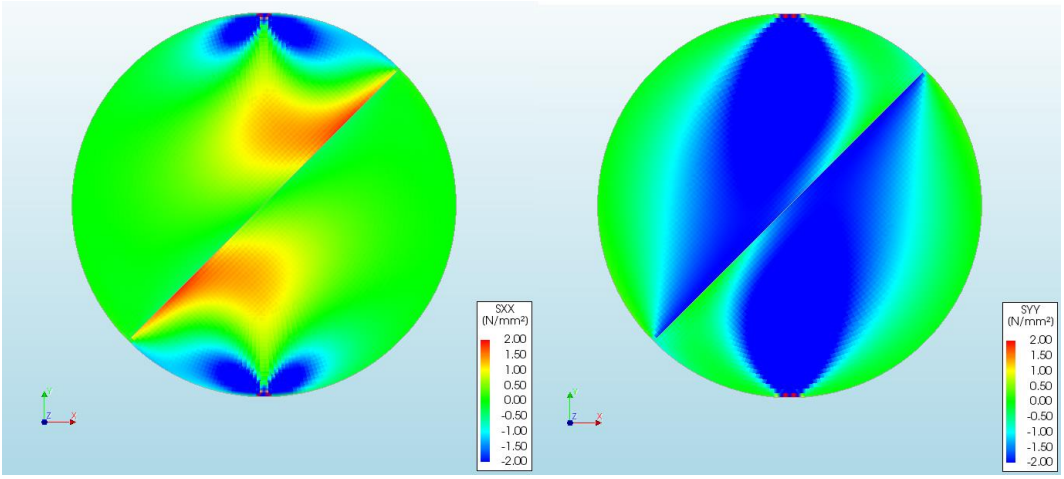

Figure 64. ***Stresses S_{xx} and S_{yy} for the specimens tested at 45º.***

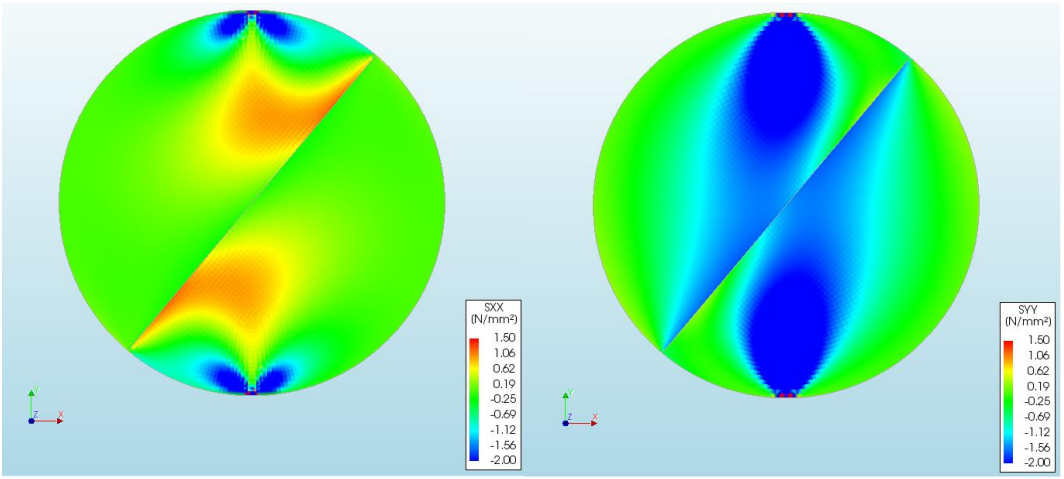

Figure 65. ***Stresses S_{xx} and S_{yy} for the specimens tested at 50º.***

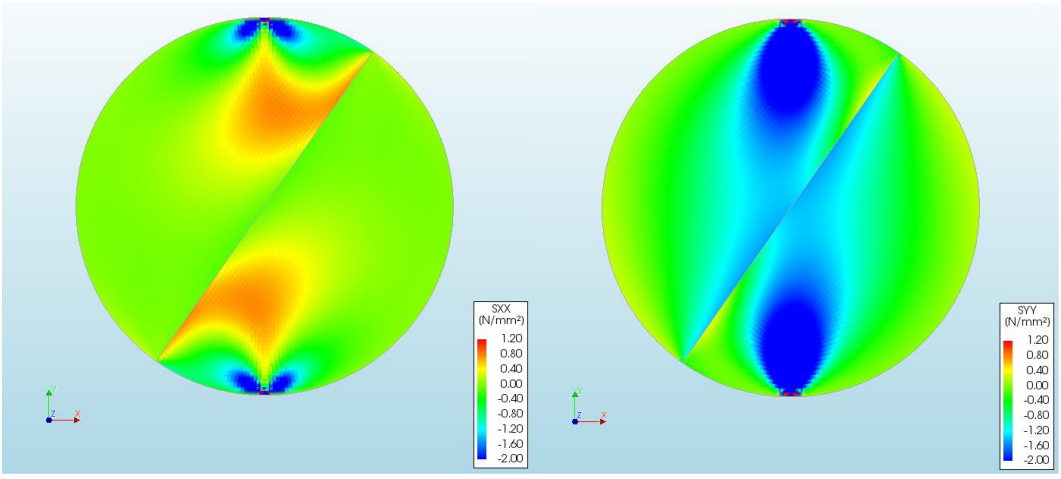

Figure 66. ***Stresses S_{xx} and S_{yy} for the specimens tested at 55º.***

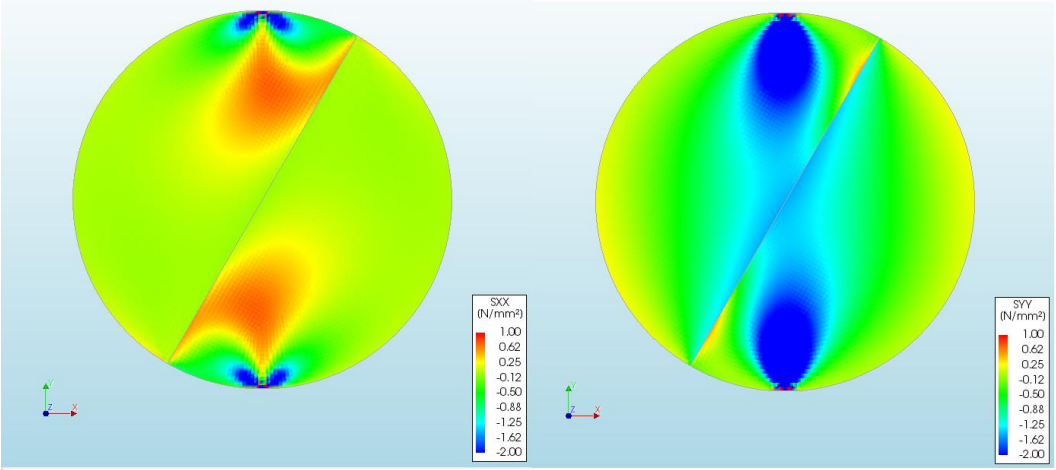

Figure 67. ***Stresses S_{xx} and S_{yy} for the specimens tested at 60º.***

5.2.2 Pelà et al. (2017)

The following figures present the stresses S_{xx} and S_{yy} for the specimens tested at 40º, 45º and 50º simulating the test carried out by Pelà, et al. (2017).

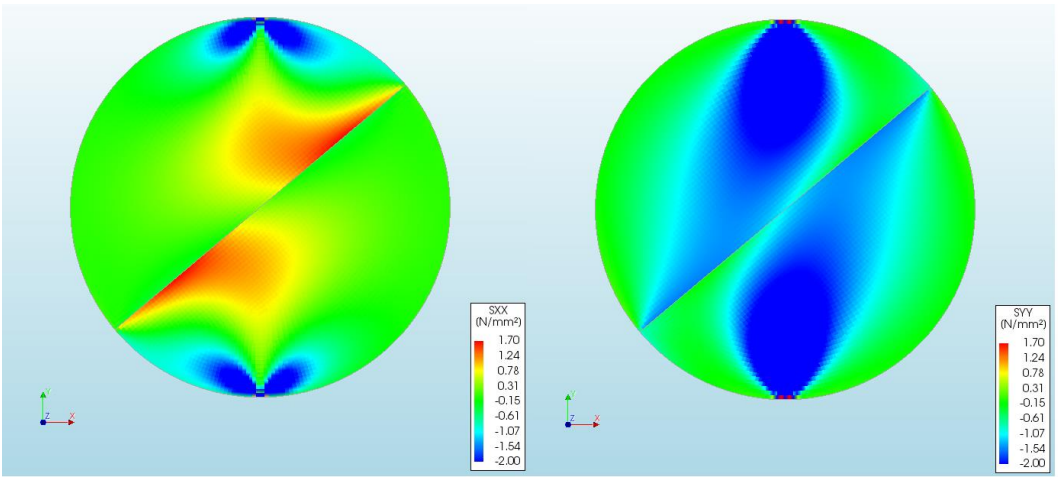

Figure 68. ***Stresses S_{xx} and S_{yy} for the specimens tested at 40º.***

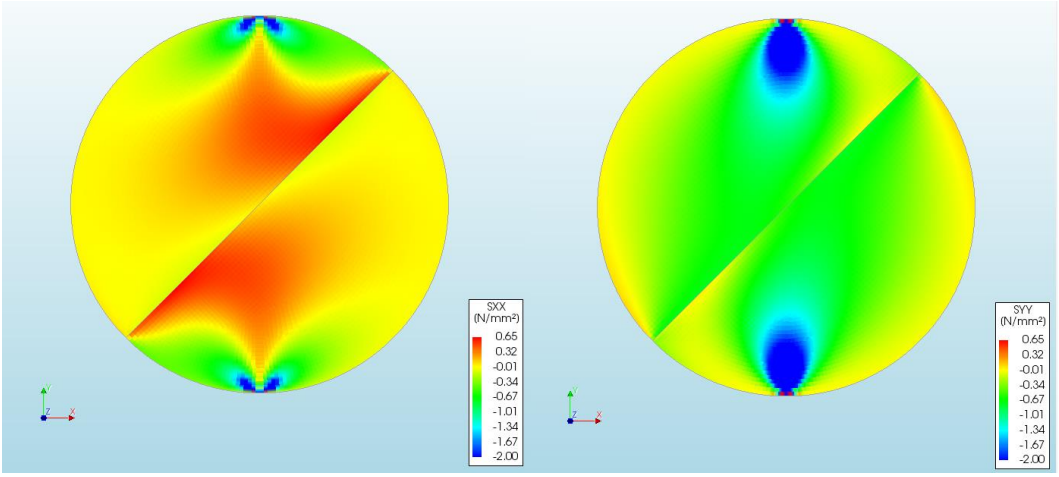

Figure 69. ***Stresses S_{xx} and S_{yy} for the specimens tested at 45º.***

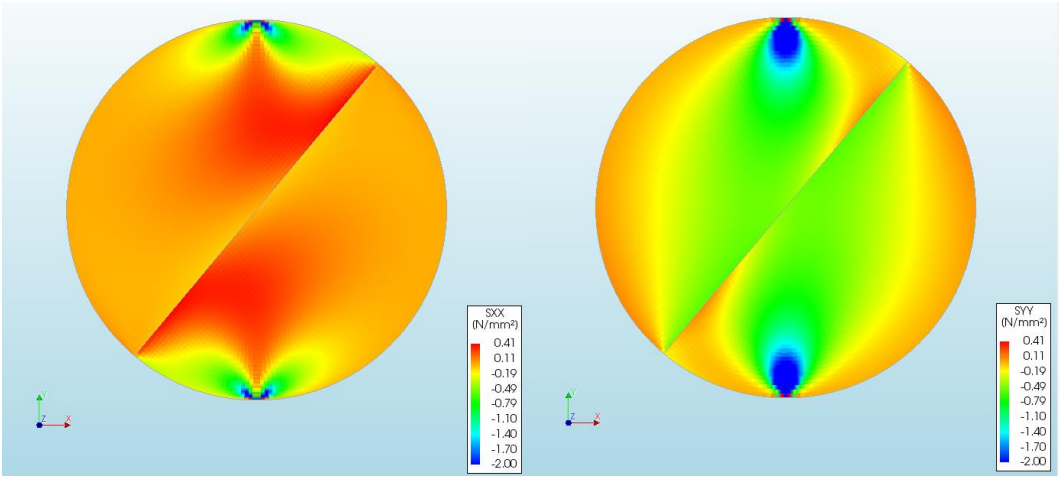

Figure 70. ***Stresses S_{xx} and S_{yy} for the specimens tested at 50º.***

Analyzing the results obtained for the vertical stresses S_{yy} and the horizontal stresses S_{xx}, it is observed that there is a **vertical compression and horizontal tension right under the applied load and above the embedment**. This behavior was clearly expected.

It is also observed that **the distribution of the stresses is antisymmetric with respect to the interface**. This is because of the inclination of the mortar-brick interface; note that the bigger the inclination, the more antisymmetric. In the limit, with a horizontal interface (0º), the distribution of stresses would by symmetric.

5.3 Stress distribution along the interface

In this section, the stresses along the interface with respect to the local axis X' (STSx) and Y' (STNy) are presented. Again, th**e stresses presented correspond to the step in which the peak strength for the given sample is reached**, i. e. before failure. A discussion of the results is also presented at the end of the section.

5.3.1 Marastoni et al. (2016)

The following figures present the stresses in the local axis of the interface for the simulation of Marastoni et al. (2016).

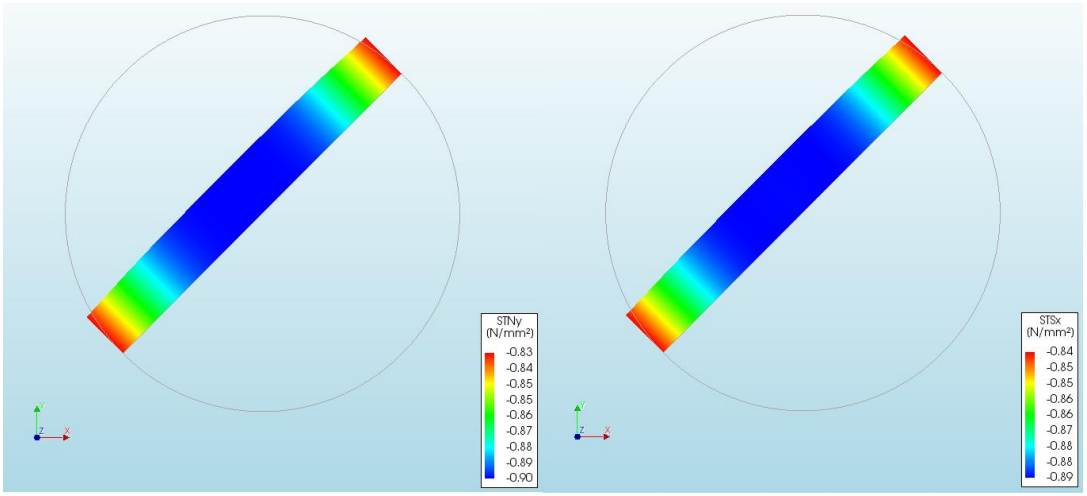

Figure 71. ***Stresses σ (STNy) and τ (STSx) for the specimens tested at 45º.***

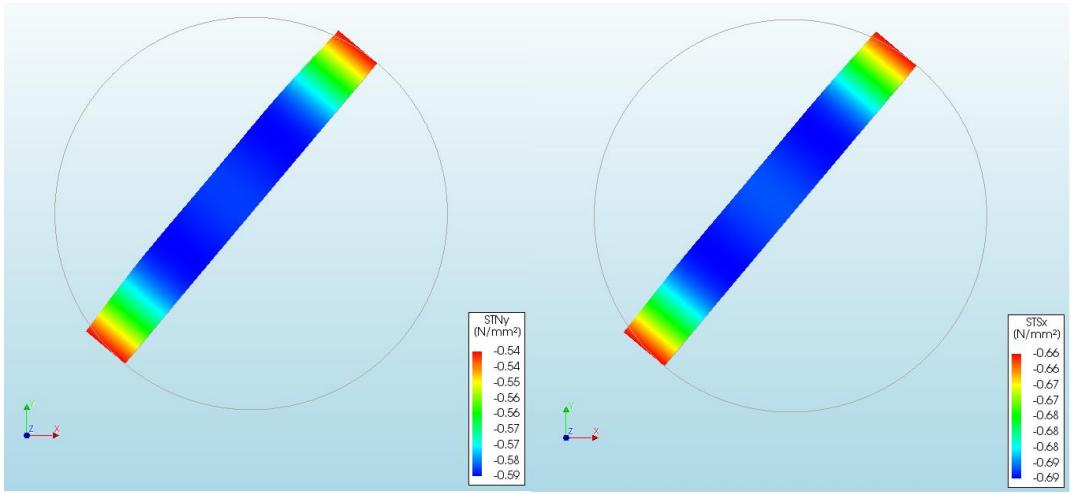

Figure 72. ***Stresses σ (STNy) and τ (STSx) for the specimens tested at 50º.***

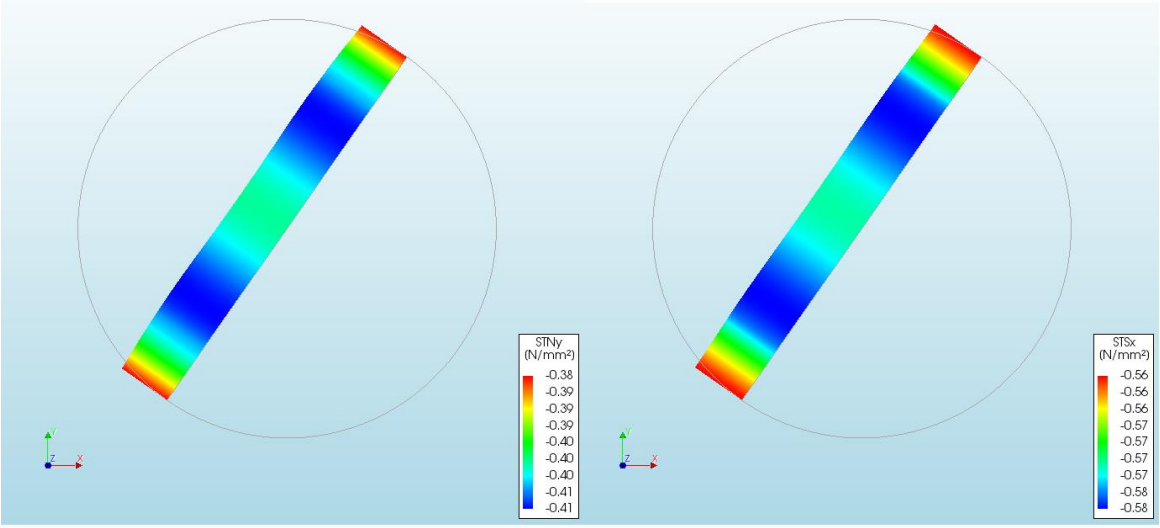

Figure 73. ***Stresses σ (STNy) and τ (STSx) for the specimens tested at 55º.***

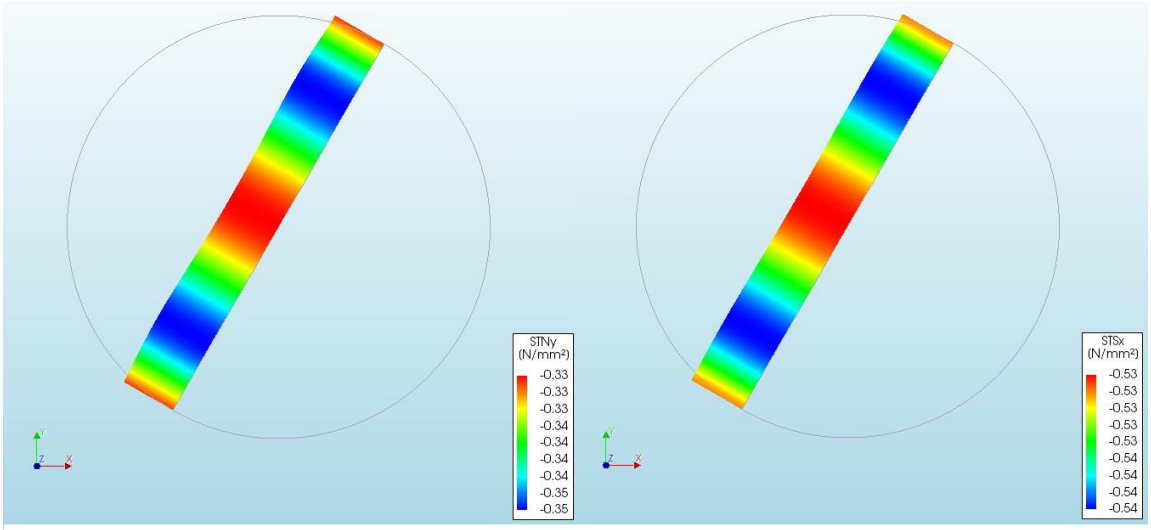

Figure 74. ***Stresses σ (STNy) and τ (STSx) for the specimens tested at 60º.***

5.3.2 Pelà et al. (2017)

The following figures present the stresses σ and τ for the specimens tested at 40º, 45º and 50º simulating the test carried out by Pelà, et al. (2017).

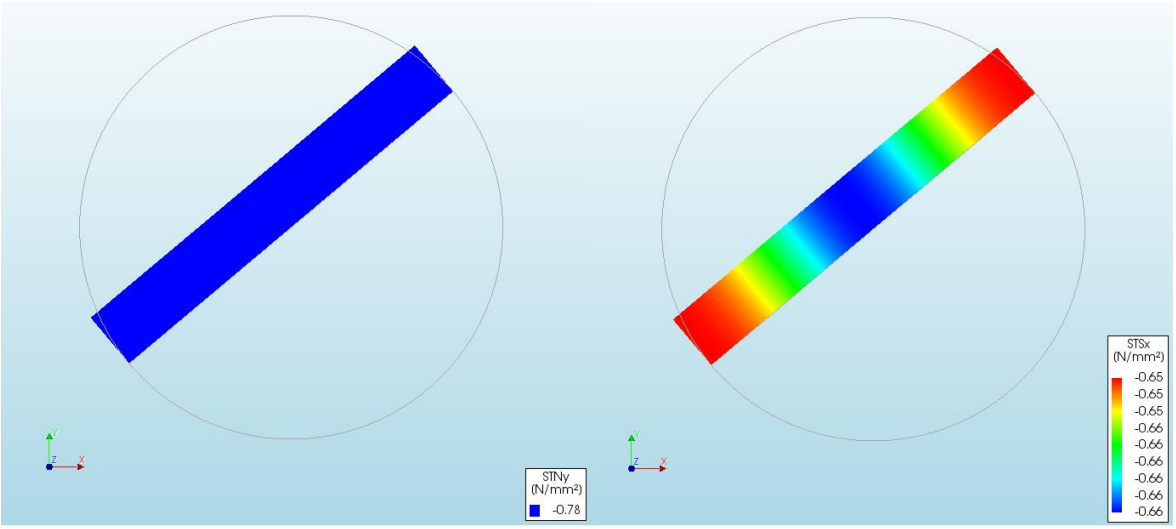

Figure 75. ***Stresses σ (STNy) and τ (STSx) for the specimens tested at 40º.***

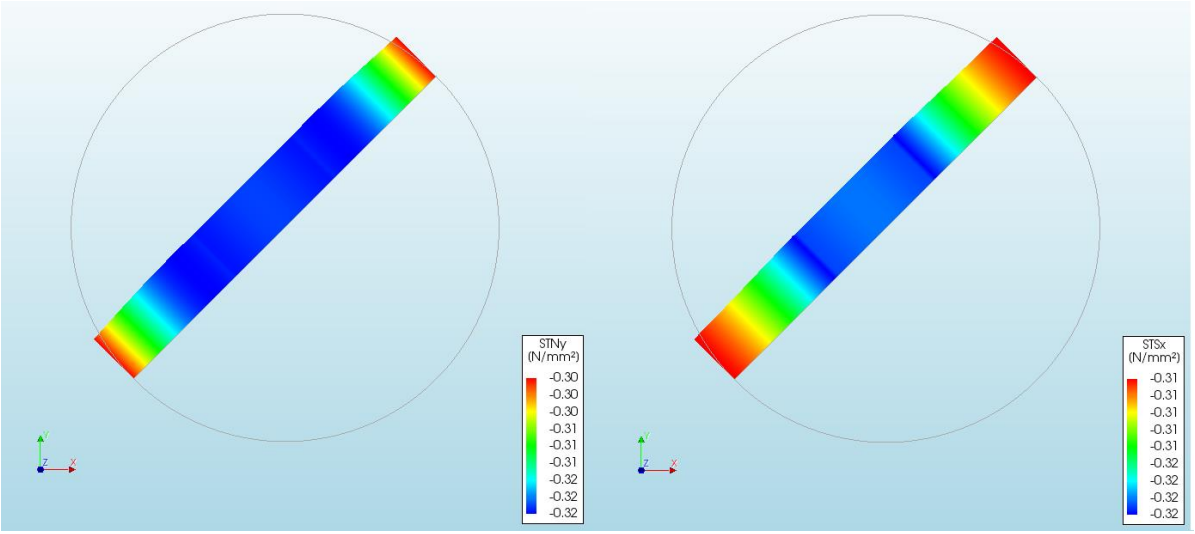

Figure 76. ***Stresses σ (STNy) and τ (STSx) for the specimens tested at 45º.***

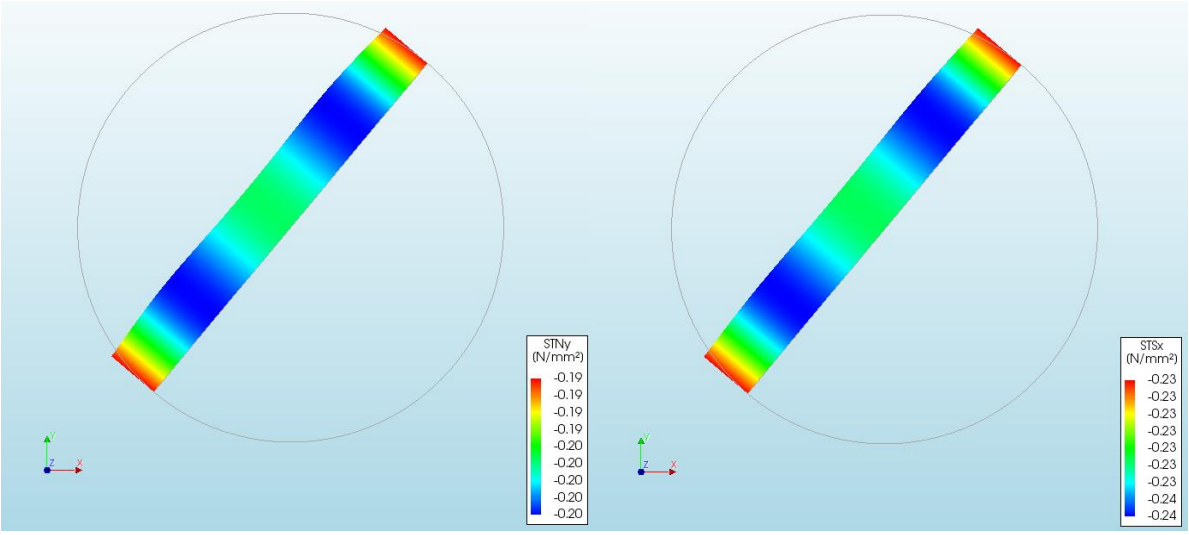

Figure 77. ***Stresses σ (STNy) and τ (STSx) for the specimens tested at 50º.***

The results show that the differences in terms of normal and tangential stress obtained along the interface are very small. This means that, according to the model, **the Brazilian tests distributes uniformly the stress along all the interface of the specimen**.

5.4 Comparison between the experimental and numerical failure envelopes

This section is one of the main important of the thesis to confirm the good behavior of the model. To do so, some background theory presented in the previous chapters will be recalled.

5.4.1 Assessment of the simulation for the campaign of Marastoni et al. (2016)

Once the results for the different angles have been obtained, the corresponding maximum shear and normal stresses are plotted in the *Shear stress – Normal stress* diagram to prove that the parameters obtained from the experimental campaigns (friction angle ϕ, cohesion c, tensile strength f_t and compressive strength f_c) behave as expected.

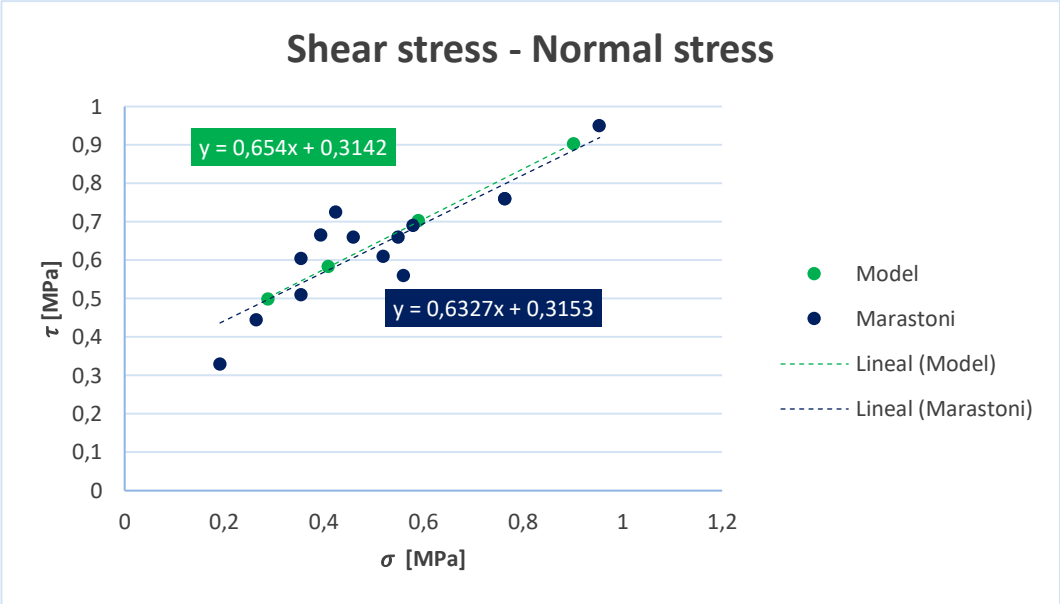

Figure 78. ***Shear stress – Normal stress diagram.***

Figure 78 shows a great performance of the model regarding the data provided by Marastoni et al. (2016):

- The cohesion of the model is **0,314 MPa** whilst the obtained from Marastoni et al. (2016) was **0,315 MPa**.
- The friction angle predicted by the model corresponds to **33,18º** (tan(33,18º)=0,654) whilst the obtained from Marastoni et al. (2016) was **32,32º**.

5.4.2 Assessment of the simulation for the campaign of Pelà et al. (2017)

The same procedure is followed for the simulation of the campaign developed by Pelà et al. (2017), obtaining the following results:

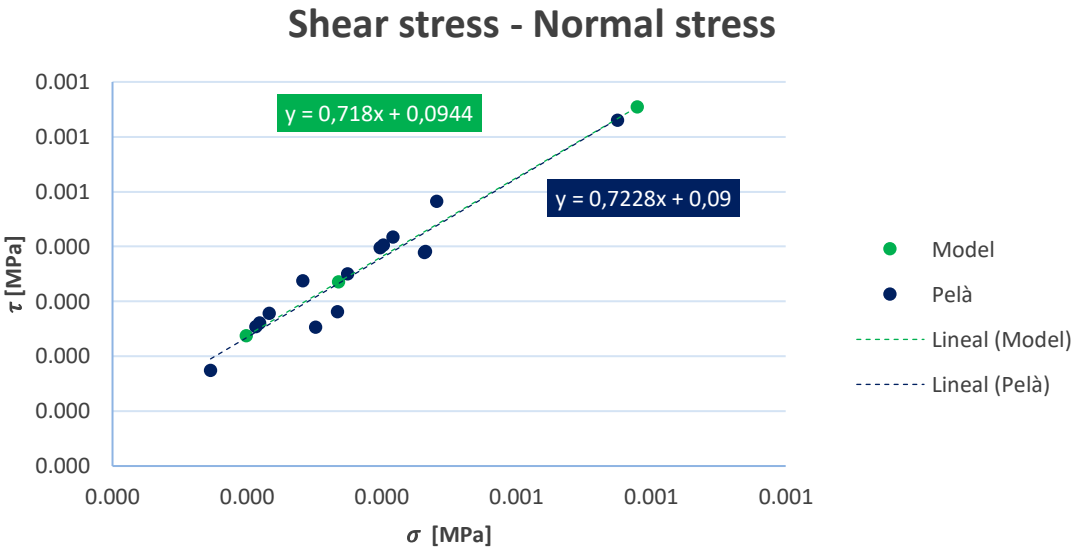

Figure 79. ***Shear stress – Normal stress diagram.***

Figure 79 shows also a great behavior for the simulation of Pelà, et al. (2017). In this case:

- The cohesion obtained with the model is **0,094 MPa** whilst the obtained from Pelà, et al. (2017) was 0**,090 MPa**.
- The friction angle predicted by model corresponds to **35,68º** whilst the obtained from Pelà, et al. (2017) was **35,86º**.

With these demonstrations, the model could be considered calibrated since it responds with a remarkable accuracy to the inputs provided by the experimental campaigns.

However, one more issue is treated in detail in this section: the **meaningful influence of the Factor C_s** in the model of the tests by Pelà et al. (2017). Prior to the discussion of this influence, two previous figures already presented in this thesis are recalled:

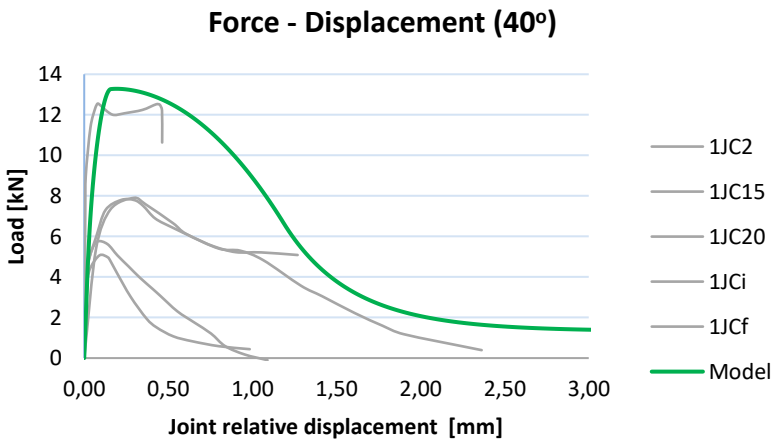

Figure 80. ***Load – Displacement curves (40º) for the simulation of the experimental campaign of Pelà et al. (2017).***

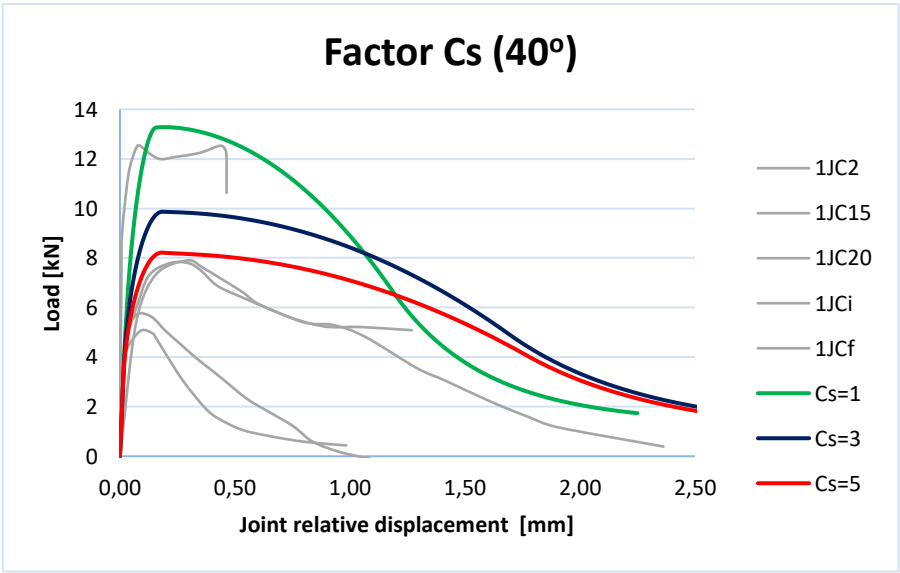

Figure 81. ***Factor Cs sensibility analysis for the simulation of the experimental campaign of Pelà et al. (2017).***

Figure 80 shows that the model clearly overestimates the strength of the joint since the peak of the numerical model is above all the experimental measurements. At the same time, Figure 81, shows that by increasing the parameter Factor C_s the strength is reduced and the correlation with the experimental data is increased. One could say

that **the best option would have been to choose $C_s = 5$**, considering these two figures. Actually, the best accuracy is obtained for $C_s = 9$, even further from the actual value proposed for the model so far ($C_s = 1$). This has an explanation:

In the first calibration carried out by the author of this thesis, Factor C_s was taken precisely equal to 9 since it was the value that provided the best accuracy. All the results presented up to this point were obtained and the model was considered as calibrated with $C_s = 9$.

However, a final last check was performed in order to validate the model: the repetition of the elemental exercise described in "4.1.6. Elemental test" with the calibrated data. For some reason, when $C_s = 9$ was used in this dummy exercise, the model didn't work well. Investigating this issue and recalling the definition of C_s, the reason was found.

Remember that C_s is the parameter that controls the shear traction contribution to compressive failure. Searching in the DIANA manuals, it is defined by the following relation (DIANA, 2017):

$$\tau = \sqrt{\frac{(f_c^2 - \sigma^2)}{C_s}} \qquad \text{Equation 27}$$

Then, the $\tau - \sigma$ diagram for $C_s = 9$ is the following:

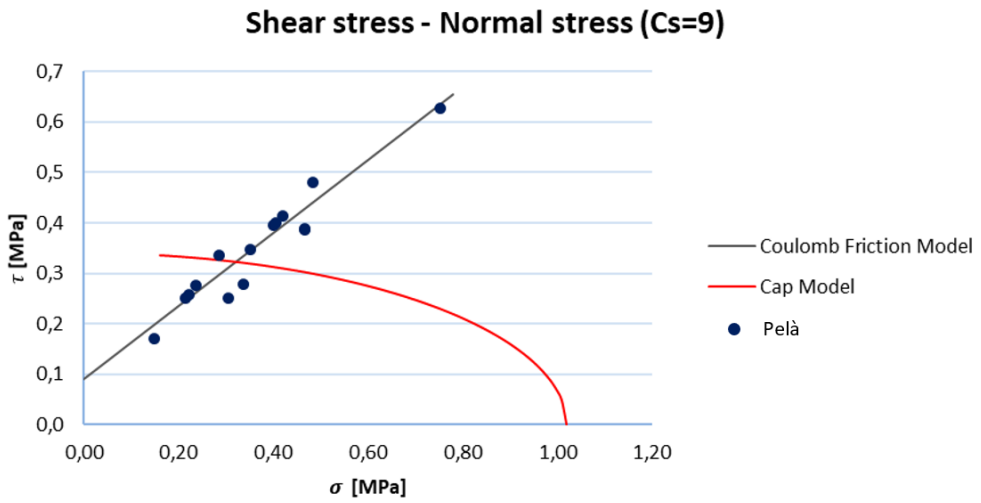

Figure 82. ***Shear stress – Normal stress for Cs=1.***

The consequence of Figure 82 is that $C_s = 9$ **is not possible** since half of the measurements of Pelà, et al. (2017) would remain out of the surface defined by the Coulomb Friction Model plus the Cap Model.

On the contrary, for $C_s = 1$ all the measurements (or properly speaking, their regression) fall inside the multi-surface model:

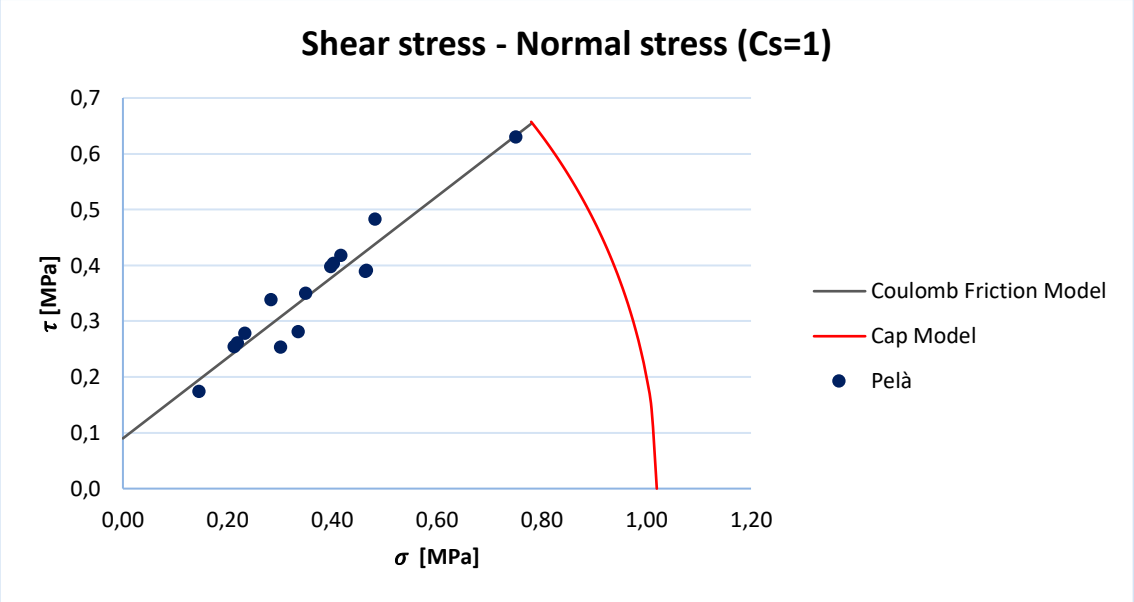

Figure 83.*Shear stress – Normal stress for Cs=1.*

This is a remarkable issue, since in many papers in the literature consulted during this thesis, the **authors use values for factor C_s that are not consistent** with their own experimental data if the “elemental test” is performed.

Chapter 6. Conclusions

6.1 Summary of the thesis

The model developed in this study has served to **investigate the behavior of masonry cylindrical specimens subjected to shear stresses**. The agreement between the numerical results and the experimental campaign entails that **the model is capable to replicate this behavior**.

The great difficulty in the modeling of the cylindrical masonry specimens subjected to Brazilian tests presented, arise both from the **uncertainty inherent to the mechanical parameters** that define the resistance of the brick-mortar joint, and the complexity in understanding the **mechanical phenomena** that occurs during the test.

In this study this complexity has been overcome with the application of **simplified micromodel that threats the brick-mortar joint as a zero-thickness interface**. The material model consisted in a multi-surface interface model also known “Composite Interface Model” developed by Lourenço (Lourenço, 1996).

In the context of numerical models, this works shows a path in which more detailed models could be used in order to obtain further results that bring more knowledge to the state of the art of mechanical behavior of masonry under shear stresses.

6.2 Conclusions of the research

In the light of the results obtained and the observations made along the present study, it is possible to draw the following conclusions:

- Analyzing the *Load – Displacement* curves provided by the simulations, it is observed that the model predicts a maximum resistance higher than the average obtained in the tests for the lowest angles. The opposite happens for bigger angles, where the model predicts a maximum strength lower than the average obtained in the experimental campaign. This behavior indicates that the model presented in this study **slightly overestimates the compression stress and underestimate the shear stress**.

- Analyzing the results obtained for the vertical stresses S_{yy} and the horizontal stresses S_{xx}, it is observed that, as expected, there is a vertical compression and horizontal tension right under the applied load and above the embedment. It is also observed that **the distribution of the stresses is antisymmetric with respect to the interface**. The bigger the inclination, the more antisymmetric is the distribution of stresses.

- The distribution of stresses along the interface shows very small differences. This means that, according to the model, **the Brazilian tests distributes uniformly the stress along all the interface of the specimen**.

- The analysis of the influence of Factor C_s indicates that even when models seem to perform in great agreement with the experimental measurements, it is useful to **carry out elemental tests**, before and after the calibration, in order to detect inconsistencies with the theoretical background.

- Numerical methods have proved to be powerful tools in the analysis of the behavior of masonry. It was shown the **great accuracy** that can be reached, even with simplified models.

- The nature of masonry as a **brittle** material entails a great difficulty in the calibration process due to the great dispersion in the experimental measurements. Develop a model that simulates the *Force – Displacement* curves with a good accuracy is not possible because of the **scattering** in the experimental data.

- Respect the experimental tests used for the characterization of the shear response of masonry, the analysis of the state of art pointed that the **lack of normative and standardized procedures** adds even more difficulty to the study of masonry.

6.3 Suggestions for future work

Based on the results obtained and the conclusions presented, the following suggestion for future work are presented:

- Respect the experimental tests, it is pointed out the need to characterize as many mechanical properties as possible during the experimental campaigns.

The more accurate the experimental tests are, the more accurate the numerical method can be. In this study, for instance, one of the campaigns did not provide parameters like the Poisson ratio, the elastic modulus, the shear modulus, etc. This is because the measure of these parameters is very complicated: measuring small strains in cylindrical specimens with a diameter of few centimeters, for instance, is very challenging. For this reason, it is necessary to **keep developing the experimental tests** in order to reduce the complexity in determining mechanical properties that afterwards are needed to feed the numerical models.

- Besides measuring more mechanical parameters, it would be helpful to build more regular specimens that present less scattering in the experimental results. For this purpose, the **construction techniques** during the experimental tests **could be improved and standardized**.

- Respect the numerical models, the model presented in this study is in the initial stage in the development of more accurate models. For instance, the same model presented in this study could be improved by adding the layer of mortar as a continuum element, i. e. creating a *detailed micromodel* instead of the *simplified micromodel* developed in this thesis. Finally, a 3-D model could be created to account for the triaxial state of stress that actually occurs in masonry.

- Finally, it would be interesting to study **other types of masonry** apart from the historical ones recreated in the experimental campaigns presented in this thesis.

References

Brocato, M. and Mondardini, L., 2012. A new type of stone dome based on Abeille's bond. *International Journal of Solids and Structures*, *49*(13), pp.1786-1801.

DIANA, 2017. *Manual DIANA.* [Online]
Available at: https://dianafea.com/manuals/d102/Diana.html
[Accessed 02 02 2018].

Drougkas, A., Roca, P. and Molins, C., 2016. Compressive strength and elasticity of pure lime mortar masonry. *Materials and structures*, *49*(3), pp.983-999.

Drygiannakis, M., 2017. *Investigation on the strength of spandrels in masonry façades* (Master's thesis, Universitat Politècnica de Catalunya).

Grande, E., Imbimbo, M. and Sacco, E., 2013. Finite element analysis of masonry panels strengthened with FRPs. *Composites Part B: Engineering*, *45*(1), pp.1296-1309.

Hendry, A.W., 1990. *Structural masonry*. Scholium International.

Hilsdorf, H.K., 1969. Investigation into the failure mechanism of brick masonry loaded in axial compression. *Designing engineering and constructing with masonry products*, pp.34-41.

Kulyakhtin, S. and Høyland, K.V., 2015. Ice rubble frictional resistance by critical state theories. *Cold Regions Science and Technology*, *119*, pp.145-150.

Li, J., Masia, M.J., Stewart, M.G. and Lawrence, S.J., 2014. Spatial variability and stochastic strength prediction of unreinforced masonry walls in vertical bending. *Engineering Structures*, *59*, pp.787-797.

Lourenço, P.B., 1996. A user/programmer guide for the micro-modeling of masonry structures. *Report*, *3*(1.31), p.35.

Lourenço, P.J.B.B., 1997. Computational strategies for masonry structures.

Laurenco, P.B., Rots, J.G. and Blaauwendraad, J., 1995. Two approaches for the analysis of masonry structures: micro and macro-modeling. *HERON, 40 (4), 1995*.

Lourenço, P.B., Barros, J.O. and Oliveira, J.T., 2004. Shear testing of stack bonded masonry. *Construction and Building Materials*, *18*(2), pp.125-132.

Lourenço, P.B. and Rots, J.G., 1997. Multisurface interface model for analysis of masonry structures. *Journal of Engineering Mechanics-ASCE, 7, 123, 660-668*.

Marastoni, D., Pelà, L., Benedetti, A. and Roca, P., 2016. Combining Brazilian tests on masonry cores and double punch tests for the mechanical characterization of historical mortars. *Construction and Building Materials*, *112*, pp.112-127.

Martin-Alarcon, D.C., 2016. *Optical monitoring & modelling of masonry behaviour under shear load* (Doctoral dissertation).

Miccoli, L., Oliveira, D.V., Silva, R.A., Müller, U. and Schueremans, L., 2015. Static behaviour of rammed earth: experimental testing and finite element modelling. *Materials and Structures*, *48*(10), pp.3443-3456.

Oliveira, L.M.F.D. and Corrêa, M.R.S., 2017. Numerical and experimental analysis of the shear capacity of interconnected concrete block walls. *Ambiente Construído*, *17*(3), pp.25-37.

Page, A.W., 1983. The strength of brick masonry under biaxial tension-compression. *International journal of masonry construction*, *3*(1), pp.26-31.

Pelà, L., 2009. *Continuum damage model for nonlinear analysis of masonry structures* (Doctoral dissertation, Università degli studi di Ferrara).

Pelà, L., Cervera, M. and Roca, P., 2013. An orthotropic damage model for the analysis of masonry structures. *Construction and Building Materials*, *41*, pp.957-967.

Pelà, L., Kasioumi, K. and Roca, P., 2017. Experimental evaluation of the shear strength of aerial lime mortar brickwork by standard tests on triplets and non-standard tests on core samples. *Engineering Structures*, *136*, pp.441-453.

Pelà, L., Roca, P. and Benedetti, A., 2016. Mechanical characterization of historical masonry by core drilling and testing of cylindrical samples. *International Journal of Architectural Heritage*, *10*(2-3), pp.360-374.

Petracca, M., Pelà, L., Rossi, R., Zaghi, S., Camata, G. and Spacone, E., 2017. Micro-scale continuous and discrete numerical models for nonlinear analysis of masonry shear walls. *Construction and Building Materials*, *149*, pp.296-314.

Pluijm, R.R., 1999. *Out-of-plane bending of masonry: behaviour and strength* (Doctoral dissertation, Technische Universiteit Eindhoven).

Roca, P., Cervera, M. and Gariup, G., 2010. Structural analysis of masonry historical constructions. Classical and advanced approaches. *Archives of Computational Methods in Engineering*, *17*(3), pp.299-325.

Rocscience, 13. *Rocscience.* [Online]
Available at:
https://www.rocscience.com/documents/hoek/corner/05_Shear_strength_of_discontinuities.pdf
[Accessed 2018 05 13].

Saloustros, S., Pelà, L., Cervera, M. and Roca, P., 2017. Finite element modelling of internal and multiple localized cracks. *Computational mechanics*, *59*(2), pp.299-316.

Sattar, S., 2013. *Influence of masonry infill walls and other building characteristics on seismic collapse of concrete frame buildings* (Doctoral dissertation, University of Colorado at Boulder).

Scheen, M.M., Experimental and numerical simulations of various unreinforced masonry walls with openings under in-plane static cyclic loading conditions.

Seller, D., 2015. *Slideplayer.* [Online]
Available at: http://slideplayer.com/slide/3277424/
[Accessed 25 05 2018].

Singhal, V. and Rai, D.C., 2014. Suitability of half-scale burnt clay bricks for shake table tests on masonry walls. *J. Mater. Civ. Eng*, *10*(1061), pp.644-657.

Vecchio, F.J. and Collins, M.P., 1986. The modified compression-field theory for reinforced concrete elements subjected to shear. *ACI J.*, *83*(2), pp.219-231.

Witt Espinosa, J.C., 2014. *Caracterización experimental de la resistencia al corte de en muros de obra de fábrica de ladrillo macizo* (Master's thesis, Universitat Politècnica de Catalunya).

Zhou, G.C., Rafiq, M.Y., Bugmann, G. and Easterbrook, D.J., 2006. Cellular automata model for predicting the failure pattern of laterally loaded masonry wall panels. *Journal of Computing in Civil Engineering*, *20*(6), pp.400-409.

Appendix 1

Example of an automatic report generated with DIANA FEA 10.2

Project information

Project name	Desktop/Ejercicio interfase/Interface_2.dpf
Analysis aspects	['Structural']
Model dimension	['Plane strain']
Default mesher type	HEXQUAD
Default mesher order	LINEAR
Diana version	Diana 10.2, Latest update: 2018-03-16 14:05:35
System	Windows NT 6.2 Build 9200
Model sizebox	1.0

Units

The following units are applied

Quantity	Unit	Symbol
Length	millimeter	mm
Mass	ton	T
Force	newton	N
Time	second	s
Temperature	kelvin	K
Angle	radian	rad

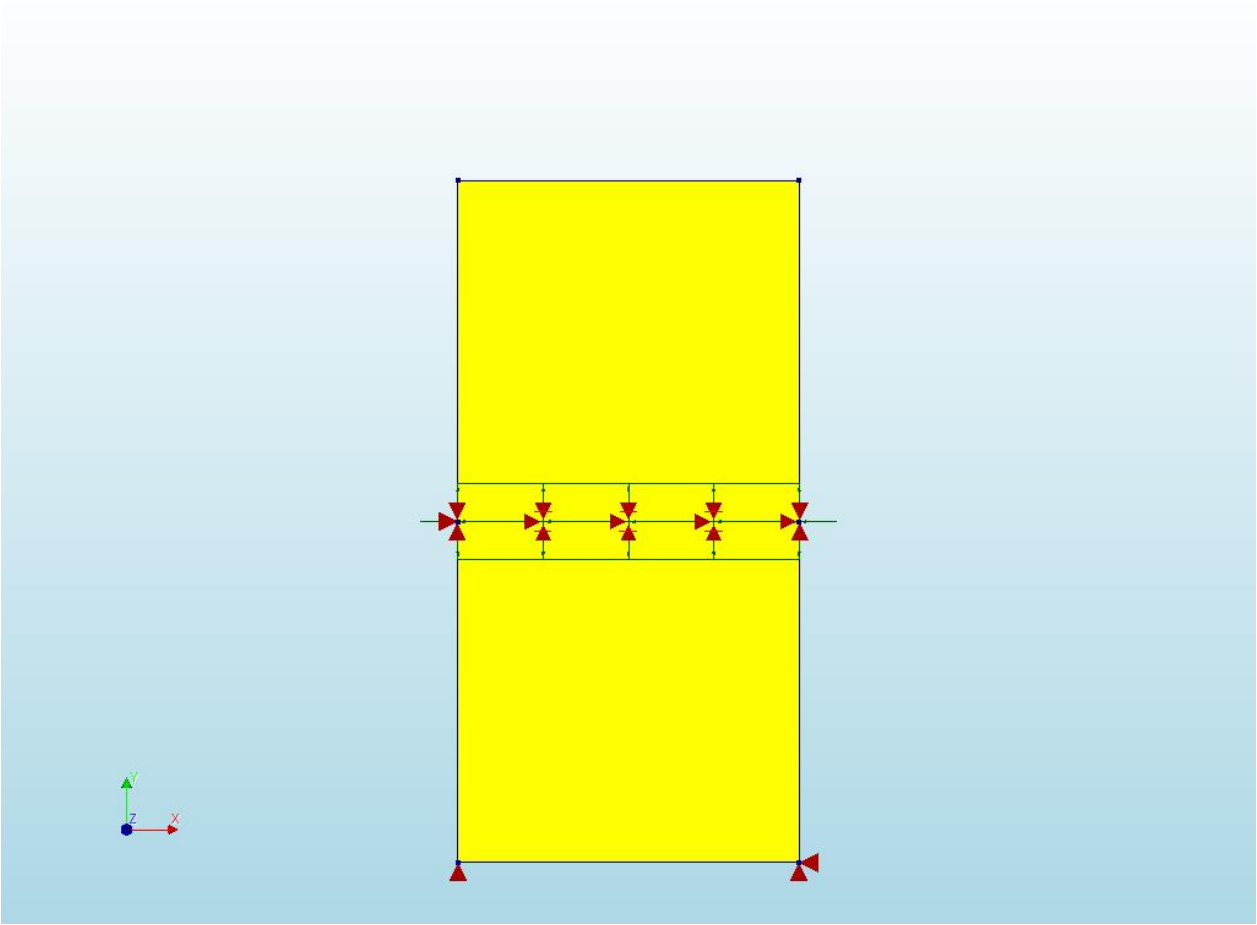

Dimensions

Axes	Minimum coordinate [mm]	Maximum coordinate [mm]
X	0.00	100.00
Y	-100.00	100.00
Z	0.00	0.00

Material: Brick

Name	Value
Material class	Concrete and masonry
Material model	Linear elastic isotropic
Color	grey
Young's modulus	9792 N/mm2
Poisson's ratio	0.15
Mass density	2.4e-09 T/mm3

Material: Interface

Name	Value
Material class	Interface elements
Material model	Combined cracking-shearing-crushing
Color	silver
Type	2D line interface
Normal stiffness modulus-y	27.8 N/mm3
Shear stiffness modulus-x	10.66 N/mm3
Tensile strength	0.35 N/mm2
Fracture energy	0.01 N/mm
Cohesion	0.32 N/mm2
Friction angle	0.5641 rad
Dilatancy angle	0 rad
Residual friction angle	0.5077 rad
Confining normal stress	-1.5 N/mm2
Exponential degradation coefficient	1
Mode-II fracture energy	0 0.23
Compressive strength	2.32 N/mm2
Factor Cs	1
Compressive fracture energy	0.35 N/mm
Equivalent plastic relative displacement	0.15